






Review

Nanoengineering of Catalysts for Enhanced Hydrogen Production

Jhonatan Luiz Fiorio ¹, Maitê Lippel Gothe ², Emerson Cristofer Kohlrausch ³, Maria Luísa Zardo ², Auro Atsushi Tanaka ⁴, Roberto Batista de Lima ⁴, Anderson Gabriel Marques da Silva ⁵, Marco Aurélio Suller Garcia ^{4,*}, Pedro Vidinha ^{2,*} and Giovanna Machado ^{3,*}

¹ Theoretische Chemie, Technische Universität Dresden, 01062 Dresden, Germany; jhonatan_luiz.fiorio@tu-dresden.de

² Institute of Chemistry, University of São Paulo, São Paulo 05508-000, Brazil; maite.gothe@usp.br (M.L.G.); malu.zardo@gmail.com (M.L.Z.)

³ Laboratory of Microscope and Microanalysis, Northeast Center for Strategic Technologies, Recife 50740-540, Brazil; emerson.kohl@gmail.com

⁴ Departamento de Química, Centro de Ciências Exatas e Tecnologia, Universidade Federal do Maranhão, São Luís 65080-805, Brazil; tanaka.auro@ufma.br (A.A.T.); rb.lima@ufma.br (R.B.d.L.)

⁵ Departamento de Engenharia Química e de Materiais, Pontifícia Universidade Católica, Rio de Janeiro 22451-900, Brazil; agms@puc-rio.br

* Correspondence: marco.suller@ufma.br (M.A.S.G.); pvidinha@iq.usp.br (P.V.); giovanna.machado@cetene.gov.br (G.M.)



Citation: Fiorio, J.L.; Gothe, M.L.; Kohlrausch, E.C.; Zardo, M.L.; Tanaka, A.A.; de Lima, R.B.; da Silva, A.G.M.; Garcia, M.A.S.; Vidinha, P.; Machado, G. Nanoengineering of Catalysts for Enhanced Hydrogen Production. *Hydrogen* **2022**, *3*, 218–254. <https://doi.org/10.3390/hydrogen3020014>

Academic Editor: Rufino M. Navarro Yerga

Received: 29 April 2022

Accepted: 17 May 2022

Published: 23 May 2022

Publisher's Note: MDPI stays neutral with regard to jurisdictional claims in published maps and institutional affiliations.



Copyright: © 2022 by the authors. Licensee MDPI, Basel, Switzerland. This article is an open access article distributed under the terms and conditions of the Creative Commons Attribution (CC BY) license (<https://creativecommons.org/licenses/by/4.0/>).

Abstract: Hydrogen (H₂) has emerged as a sustainable energy carrier capable of replacing/complementing the global carbon-based energy matrix. Although studies in this area have often focused on the fundamental understanding of catalytic processes and the demonstration of their activities towards different strategies, much effort is still needed to develop high-performance technologies and advanced materials to accomplish widespread utilization. The main goal of this review is to discuss the recent contributions in the H₂ production field by employing nanomaterials with well-defined and controllable physicochemical features. Nanoengineering approaches at the sub-nano or atomic scale are especially interesting, as they allow us to unravel how activity varies as a function of these parameters (shape, size, composition, structure, electronic, and support interaction) and obtain insights into structure–performance relationships in the field of H₂ production, allowing not only the optimization of performances but also enabling the rational design of nanocatalysts with desired activities and selectivity for H₂ production. Herein, we start with a brief description of preparing such materials, emphasizing the importance of accomplishing the physicochemical control of nanostructures. The review finally culminates in the leading technologies for H₂ production, identifying the promising applications of controlled nanomaterials.

Keywords: hydrogen; nanomaterials; controlled synthesis; nanoengineering; nanocatalysis; hydrogen production technologies

1. Introduction

Hydrogen has been considered one of the most promising and flexible energy powers that can provide heat, transport energy, and electricity by fuel cells, to name just a few [1,2]. However, it is mainly found in compounds rather than in its free state, which implies using technologies to prepare it, demanding high amounts of energy [3]. Today, there are four main sources for the commercial production of H₂ with economic benefits, which are as follows: natural gas, oil, coal, and electrolysis [4]. Among them, electrolysis is considered to present a lower environmental impact from a life cycle assessment perspective; nevertheless, this process has not reached the commercial maturity of other technologies yet [5]. Thus, the high costs, energy consumption, and technical complications prevent the widespread use

of H_2 . These are the reasons why H_2 consumption is dominated by fertilizer production in the ammonia industry, oil refining, methanol obtaining, and iron and steel manufacturing currently [6], i.e., the molecule is just used in sectors where it is indispensable. However, many efforts have been put into finding alternative hydrogen sources; among various, we can highlight biomass, microbial electrolytic cells, biophotolysis, and light-driven processes. In addition, alternative energy sources, such as solar, wind, geothermal, or nuclear, are currently being used to produce hydrogen [7–10].

Apart from technical challenges for H_2 production, other concerns are undeniable, such as storage, transportation, safety, inclusion of the gas in the energy matrix, and greenhouse gases emissions [11,12]. However, regardless of these issues, the future widespread application of H_2 is required, as increasing the molecule content in a particular process prompts a decrease in the environmental impact and leads to greener energy sources [5,13]. As the hydrogen economy consists of catalytic and non-catalytic approaches, we herein focus on catalytic-driven methods [13]. In this scenario, a variety of nanomaterials and hybrid-catalytic components have been employed as nanocatalysts for H_2 production involving many chemical transformations, including water splitting, steam reforming, electrolysis, and water–gas shift [14]. In fact, one can notice that the interest in hydrogen has often been focused on the fundamental understanding of catalytic processes for hydrogen production and the demonstration of applicability to different strategies. However, much effort is still needed to develop high-performance technologies and advanced materials to accomplish this purpose, in which the catalytic activity depends on the properties of the material. Recent contributions in the H_2 production field, catalyzed by nanostructures with well-defined and controllable physicochemical features, are moving towards new and stimulating developments.

The growing interest in nanocatalyst preparation is firstly motivated by their large surface-to-volume ratio, which dramatically increases the number of active sites at the nanoparticles' (NPs) surface and their interaction with different molecules/organic moieties [15–19]. This has led to many possibilities for creating new materials and facilitating chemical processes. Therefore, many scientists worldwide are dealing with how to combine both homogeneous and heterogeneous catalysis to create breakthrough materials to bridge the gap between them, i.e., connecting the two fields [20]. Thus, the so-called nanoengineering is a branch of nanotechnology that provides nanostructure manipulation at the sub-nano or atomic scale levels to optimize catalytic performances. In other words, creating nanomaterials with precise control over size (quantum confinement), shape, composition (mono-, bi-, and trimetallic materials), and structure remains a major research target [21]. However, these systems are interesting as they allow us to unravel how activity varies as a function of these parameters and to obtain insights into the structure–performance relationships of a particular H_2 production method. We believe that the establishment of structure performance relationships, by unraveling key compositions and morphologies, is essential to optimize performance and enable the rational design of nanocatalysts with desired activities and selectivity for a transformation of interest. Therefore, this would allow the transition from a trial-and-error method to a design-driven approach in the hydrogen production field.

This review comprehensively summarizes the main catalytic processes for H_2 production, with a brief overview of the techniques, covering steam methane reforming, water–gas shift, electrolysis, and water-splitting, focusing on their fundamentals and most promising nanocatalysts. Although steam natural gas reforming (methane, fossil fuel) is the most industrially established process, alternative H_2 production from (electrochemical or photochemical) water splitting is promising. Furthermore, electrolysis is considered more environmentally friendly and presents a solid and rapid advance in the field, as well as some other technologies [13,22]. Thus, we start with a brief description of preparing such materials by discussing how different nanostructures' size, shape, and composition affect their activities in several H_2 production approaches, summarizing the recent discoveries in the field. Then, we turn our attention to the leading technologies for H_2 production,

identifying the promising applications of controlled nanomaterials in the field, highlighting the current challenges. Therefore, the importance of developing highly efficient and stable catalysts is discussed here. When possible, the state-of-art mechanisms based on theoretical and experimental evidence will be highlighted herein.

2. Nanoscale Design Concepts of Nanocatalysts Applied for H₂ Production

It is well-known that the origin of several unique properties of NPs arises from their differences from their bulk counterparts. Physicochemical characteristics of NPs and engineered nanocatalysts, including size, shape, composition, stability, and structure, promote intrinsic surface properties, such as increased surface area and energy and surface roughness/defects, directly affecting their catalytic performances [15]. In this context, due to the great potential for application in different H₂ production approaches, and the possibility of improving or tailoring performances, nanomaterials in a variety of sizes, shapes (spheres, cubes, octahedrons, rods, wires, plates, and others), compositions (e.g., Au, Ag, Pd, and Pt), and architectures (alloys, core-shell, hollow, etc.) have been pursued for H₂ production by different strategies, as shown in Figure 1 [23–30].

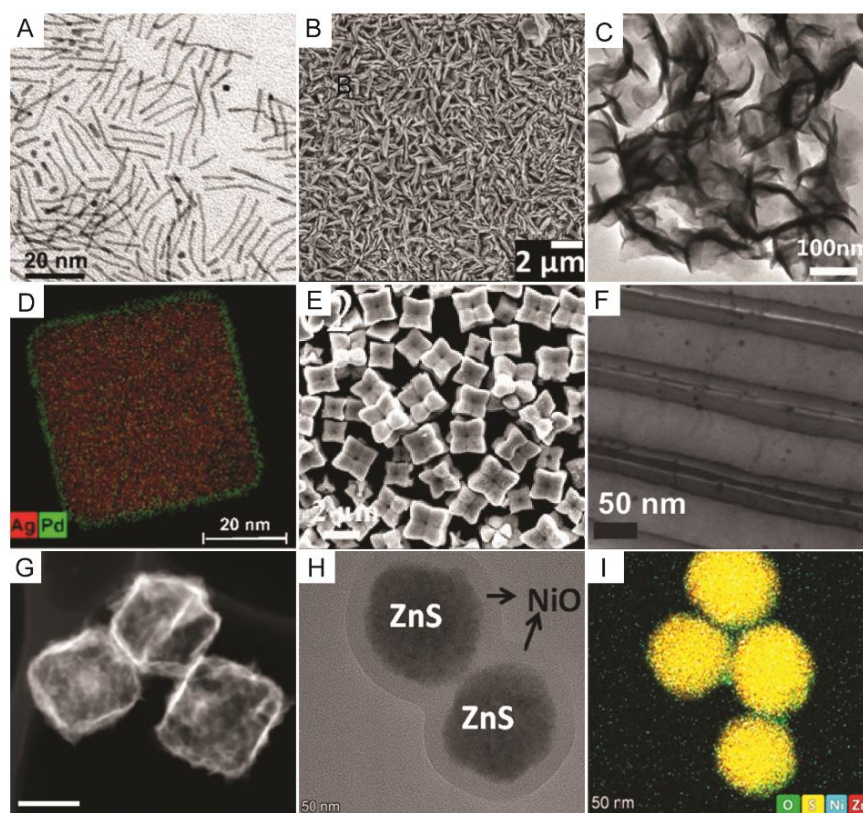


Figure 1. (A–I) SEM and TEM images for a variety of nanomaterials with controllable sizes, shapes, compositions, and structures that have been successfully reported for application in different H₂ production technologies: (A) nanorods; (B) nanoplates; (C) nanosheets; (D) nanocubes; (E) concave cubes; (F) nanotubes; (G) hollow nanocages; and (H,I) core-shell nanospheres. (A) Adapted with permission from ref. [23], Copyright 2018 American Chemical Society. (B) Adapted with permission from ref. [24], Copyright 2020 Royal Society of Chemistry. (C) Adapted with permission from ref. [26], Copyright 2013 American Chemical Society. (D) Adapted with permission from ref. [25], Copyright 2020 American Chemical Society. (E) Adapted with permission from ref. [28], Copyright 2013 Wiley-VCH. (F) Adapted with permission from ref. [27], Copyright 2017 Elsevier. (G) Adapted with permission from ref. [29], Copyright 2021 American Chemical Society. (H,I) Adapted with permission from ref. [30], Copyright 2021 Elsevier.

In this context, smaller sizes modulate the fraction of atoms on the topmost surface of the NPs, leading to higher proportions of atoms at corners, terraces, steps, and edges; also, it gives rise to quantum confinement effects. [31–33] Thus, by specifically controlling some reaction conditions (e.g., temperature, time, stirring), solvent, reducing agents, and stabilizers, it is possible to tune the size of a material, as well as other characteristics [34,35]. However, one has to bear in mind that the range of sizes matters depending on their application. For instance, the literature has comprehensively discussed gold NPs for oxidation reactions, in which NPs sizes lower than 10 nm are very efficient [18,36,37]. For H₂ production, the phenomenon can be similar, e.g., H₂ obtained via preferential CO oxidation (PrOX) showed that NP sizes lower than 10 nm presented higher performances [38]. However, when studies use gold and exploit its surface plasmon resonance (SPR), the efficiency of NPs smaller than 10 nm is low, due to the increased electron-surface collisions rate [39,40]. Zhang et al. studied the plasmonic size effect dependency on BiVO₄ photoanodes for solar water splitting, in which the maximum enhancement was found for gold NPs with a diameter of 30 nm, while the resonant photon scattering effect was only notable for sizes above 60 nm [41].

Besides size effects, NP properties are strongly dependent on their shape. Thus, the tailoring of nanostructures' performance can be achieved using versatile strategies for precisely controlling their shape [42]. Recently, Gao et al. analyzed the shape effects on photocatalytic hydrogen production via Pd/C₃N₄ photocatalysts under visible light. They prepared Pd nanocubes and Pd nano-octahedrons and demonstrated that nanostructures bound by {100} facets could significantly promote the formation of H₂, HOCH₂OH, and HCOOH, while the obtainment of the CH₃OCH₂OH product was preferred on exposed {111} facets; they also attested that photocatalytic activity improved by size reduction [43]. This effect is obtained due to differences in the surface energy of each crystal facet. According to the following Equation, surface energy (γ) can be designated as the free energy excess per unit area for producing a specific crystallographic face [44]:

$$\gamma = (1/2)N_b \epsilon \rho$$

where N_b is the number of bonds that need to be fragmented to produce the surface, ϵ is the bond strength, and ρ is the surface atoms density. Taking a face-centered cubic cell as an example (metals such as gold, silver, copper, palladium, and platinum present this cell), if we fix a lattice constant of a , the surface energies of the low-index crystallographic facets that typically encase metal nanomaterial may be assessed as $\gamma_{100} = 4(\epsilon/a^2)$, $\gamma_{110} = 4.24(\epsilon/a^2)$, and $\gamma_{111} = 3.36(\epsilon/a^2)$, indicating a surface energy sequence increasing as following: $\gamma_{111} < \gamma_{100} < \gamma_{110}$, which also could be clearly shown in Figure 2.

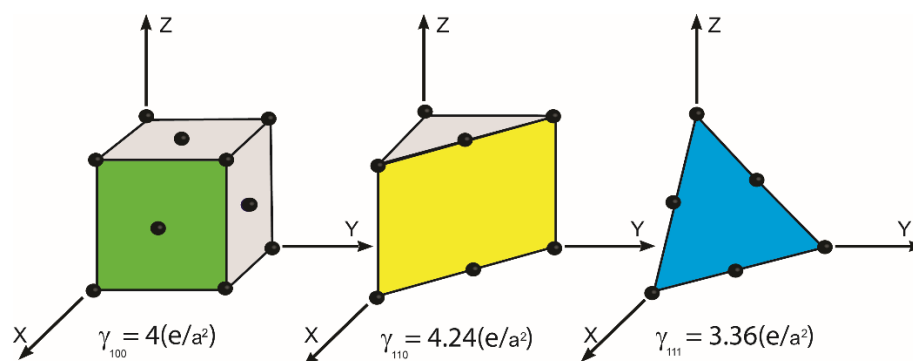


Figure 2. Surface energy value and the atomic arrangements at different nanomaterial surfaces: {100} (green), {110} (yellow), and {111} (blue) surface facets. Adapted from [45], 2012.

When one deals with bimetallic (or trimetallic) nanostructures, geometric effects also occur, but now as a function of composition, improving the interaction with the substrate. In other words, the adsorption can be modulated to be strong enough with the starting

molecule, so the reaction can occur but present weak strength with the products, so they are not bounded too intensely and can leave the catalytic site available for other substrate molecules. However, the spatial arrangement of surface atoms is not the only effect in the systems with more than one metal; specific atoms on the surface can bear different functionalities, and the interaction between elements with different electronegativities alters their electronic structure and activity. In simple terms, we are discussing the synergy effects among them [46]. Although challenging, catalyst systems' functionality arises from different designs, such as dendritic, hollow, and core-shell nanostructures, among others [47]. Thanks to the joint efforts from scientists worldwide, many protocols are available to prepare bimetallic nanomaterials, which can be extended to trimetallic systems or catalysts comprised of more than three metals [48].

Interestingly, exploiting such electronic and geometric effects emerging from the synergy of such systems, bimetallic examples are more common to find in the literature for H_2 production. For instance, Muthurasu et al. prepared hollow nanoarrays comprised of ruthenium, cobalt, and iron that presented remarkable activity in oxygen evolution, hydrogen evolution, and oxygen reduction reactions [49]. In addition, Li et al. electrochemically prepared PtRu bimetallic NPs for a pH-universal hydrogen evolution reaction with a mass current density of $109.9 \text{ mA } \mu\text{g}^{-1}$ (in $0.5 \text{ M H}_2\text{SO}_4$ at -30 mV) and $198.7 \text{ mA } \mu\text{g}^{-1}$ (in 1.0 M KOH at -100 mV) [50]. Yolk-shells spheres comprised of CoNi_2S_4 were also used for H_2 production via water splitting with high electrocatalytic activity and robust stability [51]. The synthetic procedure was a combined hydrothermal sulfidation with gas-phase phosphorization. Interestingly, the authors showed the elegant method of synthesis, in which they prepared uniform CoNi-glycerate solid spheres, from which CoNi_2S_4 yolk-shell spheres were obtained via hydrothermal conditions thioacetamide solution. Then, P- CoNi_2S_4 yolk-shell spheres were achieved by gas-phase phosphorization of the previously obtained nanostructures (Figure 3).

To close this topic, it is important to mention that plasmonic catalysis is currently at the front line in photocatalysis, since it assists the acceleration and control of several molecular transformations due to the localized surface plasmon resonance excitation [52]. Specifically, an electromagnetic wave's oscillating electric field component induces the localized collective oscillation of conduction electrons in the metal NPs, improving their performance [53]. From an environmental perspective, the possibility of harvesting energy from sunlight to transform it into chemical energy is one of the most vital points of plasmonic catalysis and is highly desired in a hydrogen economy [54]. Thus, metals such as Au, Ag, and Cu, in which the localized surface plasmon resonance excitation occurs at the visible and near-infrared ranges, have been the subject of extensive research in recent years [55]. In line with the most prominent processes in the catalysis field, the plasmonic phenomenon is strongly affected by the size, shape, and composition of the NPs. Although discussing plasmonic catalysis is not the focus of this review, we cannot disregard its importance in providing a crucial bridge from fundamental science to applications; also, we cannot ignore that the NPs' nanoengineering plays a key role in this matter, overcoming intrinsic limitations of conventional semiconductor photocatalysts [56]. In this context, recently, Mo et al., with atomic precision, tailored Au-Ag core-shell NPs for electrochemical water-splitting plasmonic H_2 evolution. Under optimized conditions, they obtained an increase of 112.5% in the efficiency of their system when compared to light-off conditions, presenting a performance 62.1% higher than the commercial Pt-based catalyst [57]. Thus, it is vital to associate physical-chemical controlling of NPs with light energy for future improved performances, which will be further discussed herein in the photochemical water-splitting reaction section.

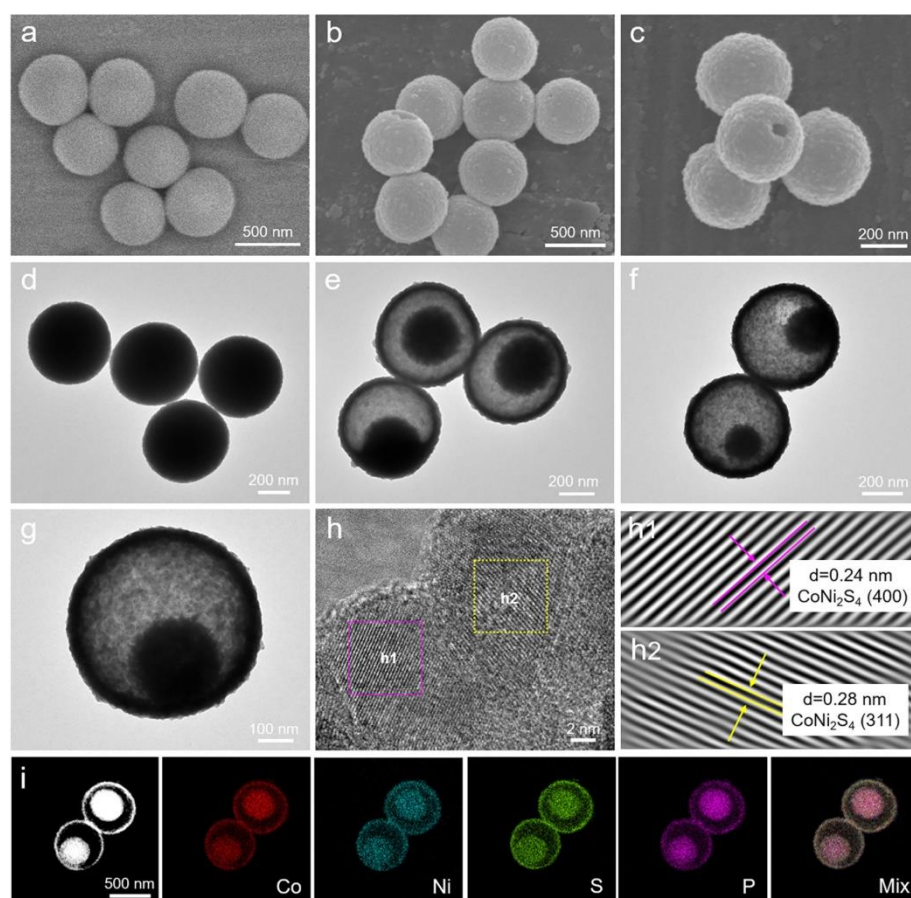


Figure 3. (a–c) Field emission scanning electrode microscopy (FESEM) and (d–g) transmission electron microscopy (TEM) images of CoNi-G solid spheres (a,d), CoNi₂S₄ yolk-shell spheres (b,e), and P-CoNi₂S₄ yolk-shell spheres (c,f,g), (h) high-resolution TEM (HRTEM) image, (h1,h2) the inverse fast Fourier transform images, and (i) elemental mapping images of PCoNi₂S₄ yolk-shell spheres. Adapted with permission from [51], Copyright 2021, Wiley.

3. Main Catalytic Processes for H₂ Generation

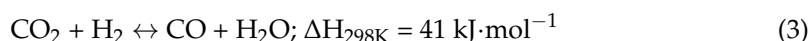
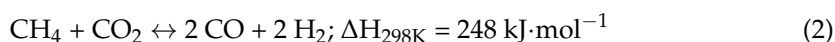
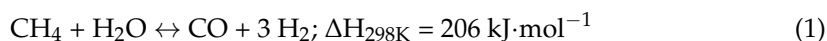
The following sections present some of the most promising catalytic methods for H₂ production. We start with methane reforming, which is well-understood and established at an industrial scale for converting natural gas into CO and H₂, but we also discuss ethanol reforming, which is a promising route for the sustainable production of H₂; then, we follow our discussions on the water–gas shift reaction. Finally, we analyze the most promising scalable alternatives to prepare H₂ with high purity, including water electrolysis and photochemical water splitting [13,58]. All the technologies include a brief introduction of the processes.

4. Methane Reforming

Natural gas reforming is the leading industrial process for H₂ production, due to its lower costs and high efficiency relative to alternative processes [20]. Although several hydrocarbons can be used, methane (CH₄), sourced from natural gas, is the most common substrate [59]. Indeed, CH₄ reforming contributes to 50% of the H₂ obtained globally [60]. Nevertheless, one must bear in mind that, although it is a near-term H₂ production and presents the benefit of producing H₂ rich in syngas, the process generates significant quantities of the greenhouse gas CO₂ [59].

Specifically, CH₄ reacts with water to yield syngas—CO and H₂—in a reaction known as steam methane reforming (SMR), as represented by Reaction 1. Moreover, syngas can also be produced by reacting CH₄ with CO₂, as defined by Reaction 2, known as dry

methane reforming (DMR). The (reverse) water–gas shift reaction (WGS or RWGS) is also noteworthy, as it occurs at equilibrium at the high temperatures employed on both SMR and DMR processes (Reaction 3), leading to similar reactor compositions [61]. In fact, in some scenarios, the same catalyst can be employed in both SMR and DMR processes, as demonstrated by Wang et al., who produced a sintering-resistant Ni@SiO₂ catalyst for both reactions [62].



The main challenges of CH₄ reforming processes are catalyst deactivation due to carbon deposition, sintering processes as high temperatures (up to 1000 °C) are usually required, and heat transfer issues that can lead to a significant temperature gradient. Indeed, the nanoscale structure of the catalyst is of great importance in avoiding coke formation, which is accomplished with the control of the particle size of the active metal and/or the support morphology [63,64]. However, from a process intensification standpoint, the heat transfer to the reaction site is not easily solved by material synthesis strategies since catalysts are generally poor thermal conductors, although they can facilitate the process [65]. Recently, Meloni et al. reported a microwave heating system for SMR, employing silicon carbide monoliths coated with a ceria/alumina slurry and impregnated with Ni, which were susceptible to microwave heat transfer. Attempts were also made by Mortensen et al., who developed CoNi NPs that were effective both as magnetic receptors for induction heating and active catalytic sites for SMR, reaching temperatures above 800 °C and CH₄ conversion rates surpassing 90% for over 300 h on stream [66].

In a recent review, Jang et al. found that both noble (Rh, Ru, Pd, Pt, and Ir) and non-noble metals (Ni and Co mainly) can be used for the DMR, wherein noble metals stand out for their lower tendency to deactivate through carbon formation, while non-noble metals are still considered despite their rapid deactivation due to their cost-effectiveness and high activity [67]. Thus, opportunities to improve their efficiency are unquestionable. They also concluded that strong metal–support interaction (SMSI) with homogeneous solid solutions, such as RhMg₂O₄, NiO-MgO, NiAl₂O₄, MgAl₂O₄, LaNiO₃, and LaSrCoO₃, leads to better dispersion and smaller sizes of active catalytic sites, which in turn leads to less deactivation by sintering or carbon deposition [67]. Zeaiter et al. obtained similar conclusions regarding the benefits of basicity and SMSI and also point out that SMSI requires regulation, since it may also increase reducing temperatures for catalytic activation as particle size decreases [68]. In this context, a review by Usman et al. on various parameters of the DMR found that nickel-based bimetallic and monometallic catalysts are the most promising alternatives to avoid catalyst deactivation due to coking [69]. In fact, Guczi et al. have shown that adding gold to a Ni/MgAl₂O₄ catalyst avoided the deposition of graphitic carbon during DMR, consequently preventing the deactivation of the catalyst [70]. Zeng et al. also managed to reduce catalyst deactivation by modifying Co/Al₂O₃ catalysts with mixed rare-earth elements, which led to an active catalyst and low carbon deposition at 800 °C during 320 h on stream [71]. Novel approaches to the DMR are also being considered, such as the plasmonic photocatalyst developed by Halas et al., which features Cu NPs acting as antennae to absorb light and reactive sites comprised of Ru single atoms (SAs) [72]. This plasmonic photocatalysis process attained 50 h of stability on stream with 99% selectivity at room temperature and atmospheric pressure, which was possible since Ru SAs do not promote RWGS and carbon deposition as other forms of Ru would do [72].

Studies on the catalysis process or catalyst design on the efficiency of methane reforming improvement/coking resistance are essential, although evaluating the materials' structure during the process is challenging, and deep knowledge of how they change during the reaction is not straightforward. However, attempts to understand the process are available in the literature. For example, Niu et al. have shown through DFT calculations and experimental kinetic data that a Pt monolayer on a Ni@Pt core-shell structure avoids carbon deposition during SMR by modifying surface electron density, leading to reactive OH* species that activate CH₄ rather than a CH₄ direct dissociation mechanism, as would occur on monometallic Ni catalysts [73]. Furthermore, Azancot et al. studied the influence of the synthesis method on the activity of Ni-Mg-Al catalysts on SMR and the level of interaction of the metals [74]. The impregnation-coprecipitation method yielded the more active catalyst by reducing NiO to Ni⁰ while still maintaining the small size of Ni⁰ NPs and their distribution, which were strongly interacting with the spinel-type MgAl₂O₄ support [74]. Nevertheless, carbon deposition was minimal at the catalyst synthesized by the coprecipitation method, which is assumed to be due to the presence of NiO-MgO solid solution on this catalyst, since the alkaline nature of MgO is known to avoid carbon deposits [74].

In addition, since carbon deposition occurs on the acid sites, basic supports were also found to avoid coking and promote the activation of weak acid CO₂ [67]. Metal oxides with reducible properties and the capacity to store oxygen (e.g., CeO₂) are preferable as supports and have been extensively studied. Interestingly, the reduction in coke formation with high oxygen storage capacities materials arises from lattice oxygen interactions with the adsorbed carbon components [75]. In addition, highly dispersing active sites over CeO₂-based catalysts were found to prevent coking, as shown by Safavinia et al. The study showed that Ni doping in CeO₂-ZrO₂ NPs improved the catalytic activity for the decomposition of methane. In this case, the authors obtained Ni on the structure by a two-step co-precipitation/molten salt synthesis, increasing oxygen vacancy concentration [76]. Knowledge regarding the effect of the CeO₂ preparation method is also available for understanding carbon deactivation. By thermal decomposition, hydrothermal, sol-gel, and precipitation techniques, the authors obtained Ni/CeO₂ catalysts for DMR; using XRD, TEM, and TPR, crystalline structural differences raised for the CeO₂ support (in which the precipitation method promoted the lowest amount of carbon formation), but also to the Ni active species, attesting that the catalyst performances were similar, with coking resistances rather different [77]. Ni et al. used commercial and homemade (hydrothermal and precipitation methods) CeO₂ as support for Ni and also evaluated the preparation methods in the system's performance. The hydrothermal material presented more oxygen vacancies and five times more initial conversion than the other two CeO₂ counterparts [78].

However, the CeO₂ support morphology plays a key role in the process, although it is still hardly exploited for methane reforming compared to other catalytic systems. Wang et al. prepared CeO₂ nanorods ({200} and {220} planes), nanocubes ({100} planes), nano-octahedrons ({110} planes), and NPs (mainly {100} planes) and used them to support Ni species for DMR (Figure 4).

Beyond the observation that Ni species were incorporated into the support lattice, occupying the vacant sites, and induced an increase in oxygen vacancies, they showed that morphology/crystal-plane affected the catalytic performance. Among them, the nanorod-based catalyst was the most efficient and stable; they attributed its superior aspects to the stronger interaction among the nanorods-shaped CeO₂ and the Ni species. They also observed that the oxygen lattice mobility and vacancies were shape-dependent and aided the carbon deposition elimination [79]. Tu et al. took a different approach to studying the reaction. They prepared CeO₂ porous flowers containing NiO NPs, which were reduced using hydrogen, and immobilized them on an alumina-silica fiber network. The nanoflowers were essential for Ni dispersion, no-aggregation at high temperature, and resistance to coke deposition. Three Ni contents (2.1, 3.4, and 4.6%) were used, and the

3.4% presented the best performance. Moreover, comparisons with a system without the flower showed that the proposed system reached enhanced conversion with less metal [80].

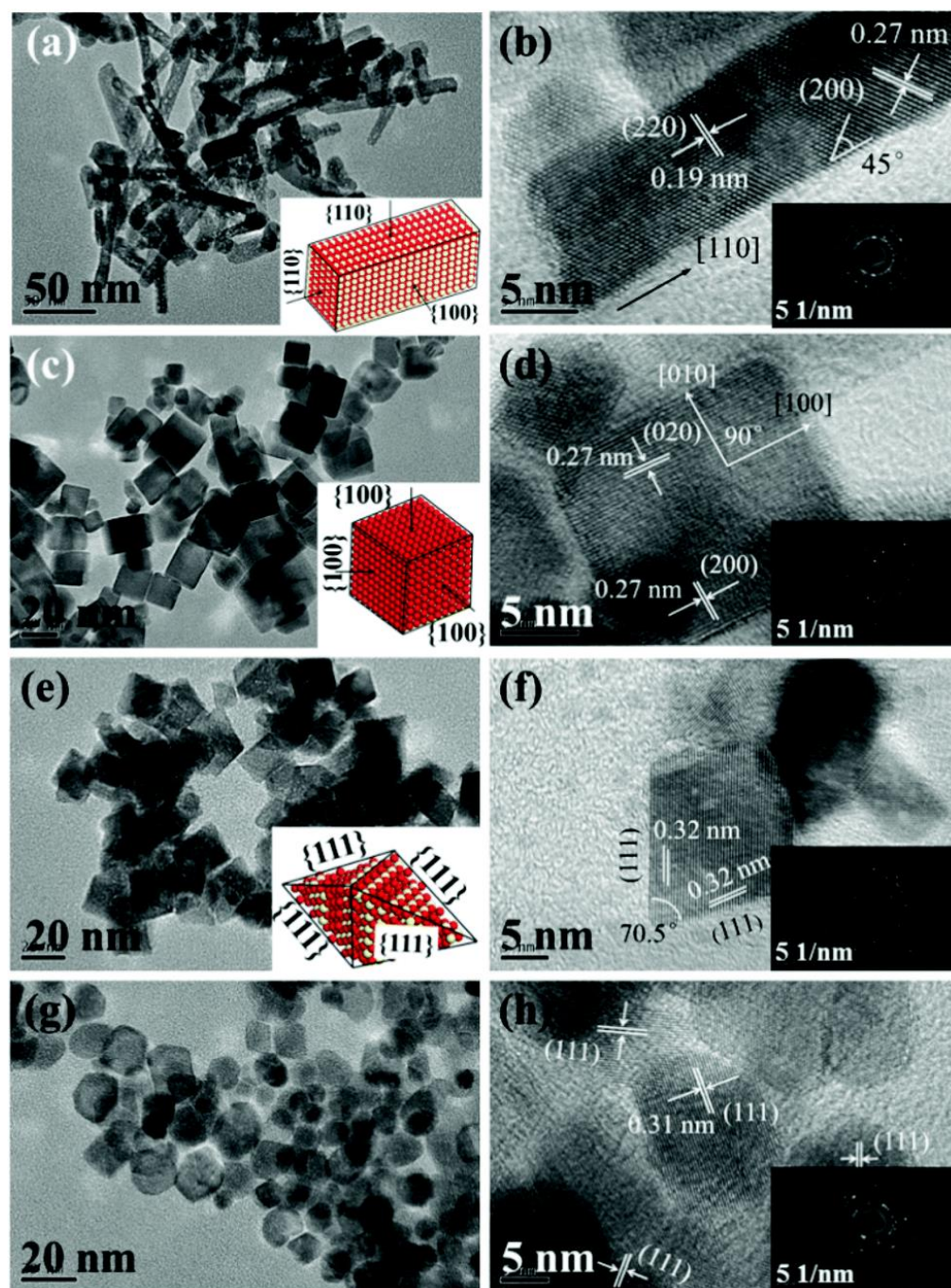


Figure 4. TEM, HRTEM, and SAED images of the different-shape CeO_2 : (a,b) nanorods, (c,d) nanocubes, (e,f) nano-octahedrons, and (g,h) NPs. Reproduced with permission from [79], Copyright 2016, Royal Society of Chemistry.

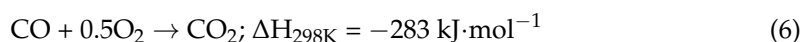
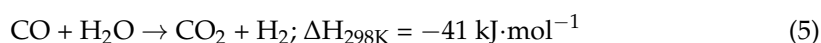
Although most of the examples presented herein with controlled supports were non-noble metal-based catalysts, noble metals were also implied for the reaction with great performances. As expected, different-shaped Ceria support is responsible for different performances; however, the metallic active phase is also essential and can completely change the tendencies observed before. In addition, similar features that were essential before are the main reasons for discussing the improved performances of some catalysts.

For example, He et al. prepared CeO₂ nanorods, bounded to {110} facets, nanocubes, bounded to {100} facets, and nanopolyhedra, bounded to {111} facets, as support for Ru NPs. The first two presented higher oxygen vacancies, a feature attributed to the main property for their increased performance [81], which were also discussed before, showing the high importance of support preparation.

Generally, all the studies are essential and systematically present the support and active species action, but it is not easy to propose a generalization. Theoretical calculations bring important insights regarding the materials/reaction conditions/metal support interactions; however, the literature does not suggest specific conditions for controlling morphology to achieve a certain performance, bringing opportunities for more profound studies.

5. Ethanol Steam Reforming (ESR)

Among liquid substrates for H₂ production, ethanol is one of the most promising and sustainable alternatives due to its renewable and biodegradable nature, high availability, low toxicity, and simple and easy transportation [82]. The ESR reaction consists of the following Reactions 4–6, under a temperature range of 200 to 650 °C at atmospheric pressure [83]:



The literature comprehensively discusses several noble or non-noble metals over a myriad of oxides for this application, not focusing on shape-controlling, although size distribution is always in the spotlight [82]. Thus, following our target, the morphology effects on ESR will be explored mainly for ceria-based catalysts due to the more profound knowledge available for their synthesis.

The catalytic role of ceria is mainly related to its redox (Ce⁴⁺/Ce³⁺) properties and the average number of oxygen vacancies due to surface defects [84]. Such features can be modulated by doping processes. For example, high dispersion of Ni NPs boosted metal–support interaction, and abundant oxygen vacancies have been accomplished by doping CeO₂ with praseodymium (Pr) with different concentrations by a sol-gel preparation. The authors achieved highly active SRE catalysts without sintering, increased coke deposition resistance following a higher concentration of oxygen vacancies, and complete ethanol conversion for more than 7200 min without activity loss at 600 °C and atmospheric pressure, when Ni was loaded on 20% Pr-doped ceria. They confirmed the increased oxygen vacancies by EPR, Raman, XPS, and DFT calculations [85]. Furthermore, lanthanum (La), terbium (Tb), and zirconium (Zr)-doped CeO₂ supported Ni catalysts were prepared by a sol-gel method, in which the adjustment of catalytic performance, metal-supported interaction, Ni dispersion, size, and surface oxygen vacancies were achieved. However, the authors described the La-doped ceria-supported Ni catalyst as pursuing the most improved properties, which were explained by DFT calculations, showing that this doping promoted more vacancy generation and facilitated the dissociation of water during the reaction [86].

Hydrogen spillover on the CeO₂ support also depends on the morphology, size, stability of Ce 4f levels, and active-phase dispersion [87]. Cobalt and nickel are considered the most promising catalysts for industrial ESR, and CeO₂ contributed significantly to their catalytic activity and stability, due to high oxygen mobility and storage capacity [88,89]. However, fundamental knowledge of catalyst deactivation, carbon deposition, reaction mechanism, sintering, metal oxidation, and metal–support interactions is lacking [90]. Shape-control procedures for preparing ceria associated with these metals are also a strategy to tune catalytic properties, stability, and long-term utilization; however, we feel that oxygen vacancies are not always discussed [91]. For example, Araiza et al. recently studied how precipitation or hydrothermal-prepared CeO₂ nanostructures (particles, rods, and cubes), when used to obtain 10 wt.% Ni/CeO₂, would affect carbon deposition during ESR. Apart

from the metal particle size and dispersion, its interaction with different-shaped ceria was essential. They discovered that Ni supported on CeO₂ rods showed improved activity and H₂ yield at 550 °C for 24 h under stream and lower amount of carbon deposits, which were attributed to the catalysts' enhanced oxygen storage capacity and Ni dispersion [92]. Moraes et al. also studied the ceria morphology (nanocube, nanorods, and flower-like) effect in Ni-based catalysts, but for low-temperature ESR and found out that the carbon formation was higher over the CeO₂ nanocubes catalyst, due to more Ni carbide phase development [93]. It is worth mentioning that similar studies were performed with metals other than Co and Ni, such as Cu over CeO₂, to attest to its performance [94].

Moreover, scientists have focused on controlling their physicochemical features by controlling their sizes, shape, composition, and structure to enhance the redox process and increase the oxygen vacancies at ceria-based catalysts. For example, it has been demonstrated that manipulating the NPs' size and shape (e.g., nanocubes, nanorods and nanowires) strongly affects their properties, making it an efficient strategy for maximizing performance [95,96]. In this case, ceria nanostructures displaying sizes below 20 nm present substantial enlargement in their cell parameters and an increased quantum confinement effect, which facilitates the reduction of Ce⁴⁺ to Ce³⁺ ions and leads to an increased amount of oxygen vacancies. In the past few years, significant advances have been achieved by linking the shape of CeO₂ supports with catalytic performance. In this context, one-dimensional CeO₂ nanostructured materials have received tremendous attention due to their unique properties derived from low dimensionality and high surface area. Our group demonstrated high-yield synthesis (>97%) of Ce_{0.9}Sm_{0.1}O_{2-δ} nanowires as an outstanding nanocatalyst support, showing superior activity, selectivity, and stability toward ethanol steam reforming. [97] The Ce_{0.9}Sm_{0.1}O_{2-δ} nanowires were employed as physical templates for the deposition of Ni by a wet impregnation method without utilizing any stabilizing agent, as shown in Figure 5A–G. [97] The Ni/Ce_{0.9}Sm_{0.1}O_{2-δ} nanowires displayed a high specific surface area, increased oxygen vacancies, and finely dispersed Ni particles with significantly higher metallic surface area than the catalysts prepared from commercial materials with similar characteristics compositions. Such singular properties were evidenced in the outstanding performances of the Ni/Ce_{0.9}Sm_{0.1}O_{2-δ} nanowires towards ethanol steam reforming (Figure 5H). The nanowires exhibited high yields for hydrogen production (~60% of selectivity) and exceptional stability, with no loss of activity after 192 h of reaction at 550 °C [97].

Noble metal-based catalysts supported on ceria are also studied, and as expected, the activate phase has a high effect, and CeO₂ shape-controlled synthesis can present a different trend than that observed for Co and Ni metals. Wang et al. prepared Ir/CeO₂ over polyhedral and nanorods ceria shapes and studied their stability and efficiency over ESR. According to the authors, they presented different performances due to water activation abilities. After stability tests at 923 K, the CeO₂ NPs kept their original shape, while the CeO₂ nanorods changed to polyhedrons. Higher ethanol conversion and hydrogen yield were obtained over the polyhedral Ir/CeO₂ catalyst, probably due to the higher migration of C₂ intermediates [98]. CeO₂ nanocubes, nanorods, and flower-like structures were used to obtain Pt/CeO₂ catalysts for ESR. The Pt/CeO₂ nanorod catalyst was the most stable, and XPS revealed that the Pt reduction is preferred on these nanostructures, due to the increased reduction of Ce⁴⁺ into Ce³⁺, which can promote a different deactivation mechanism compared to the other morphologies [99].

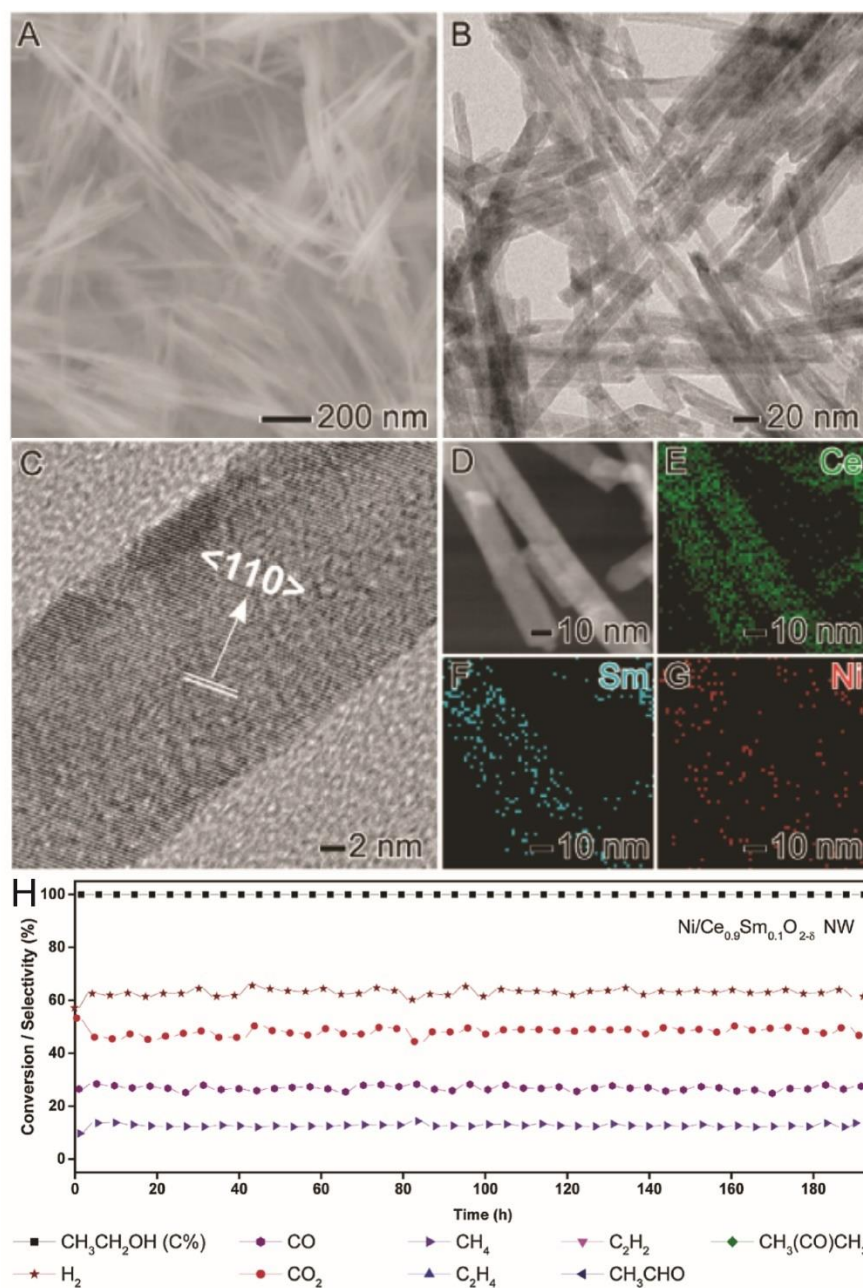
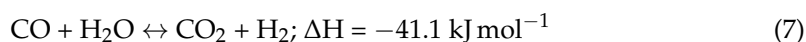


Figure 5. (A) SEM, (B,C) HRTEM, and (D–G) STEM-EDX images of Ni/Ce_{0.9}Sm_{0.1}O_{2-δ} nanowires obtained by a hydrothermal method followed by the wet impregnation of Ni. (H) Ethanol conversion and product selectivities obtained using Ni/Ce_{0.9}Sm_{0.1}O_{2-δ} nanowires as catalysts. The experiments were performed at 550 °C and H₂O/CH₃CH₂OH molar ratio = 3. Adapted with permission from ref. [97], Copyright 2019 Elsevier.

6. Water–Gas Shift Reaction

The water–gas shift (WGS) reaction, represented in Reaction 7, is an essential reaction in the industry for large-scale H₂ production [14,100–102],



Commercially, this reaction is conducted in a two-step process, which is as follows: high-temperature shift (573–723 K) over Fe–Cr based catalysts and subsequent low-temperature shift (473–523 K) over Cu–Zn catalysts [103]. Yet, these catalysts suffer from low activity and stability and require pretreatment and regeneration [14]. One

has to bear in mind that the activity of the catalysts for the WGS reaction can be further improved by microwave-assisted heating [104], high-gravity environment [105], light-assisted approach [106,107], electrochemical processes [108,109], or heat recirculation environment [110]; however, the catalyst design is essential for the success of the chosen enhancement process. Thus, different metal catalysts have been investigated, opening possibilities for future alternative industrial catalysts depending on the operating conditions; also, MSI and synergetic effects between different metals can aid the reaction. For example, under light irradiation, a $\text{CuO}_x/\text{Al}_2\text{O}_3$ (Figure 6A) catalyst containing 19 wt.% displayed outstanding catalytic activity ($122 \mu\text{mol g}_{\text{cat}}^{-1} \text{s}^{-1}$ of H_2 evolution and >95 % of CO conversion) [107]. The activity was found to be even superior to noble metal-based catalysts (Figure 6B). Significantly, this light-driven WGS process costs no electric/thermal power but attains 1.1 % of light-to-energy storage. The enhanced performance of the solar-driven WGS reaction over $\text{CuO}_x/\text{Al}_2\text{O}_3$ can be ascribed to the combined photothermocatalysis and photocatalysis (Figure 6C); nevertheless, the catalyst choice was crucial; although this material showed CO conversion similar to its Fe-based counterparts, a reduction over 200°C working temperature was possible.

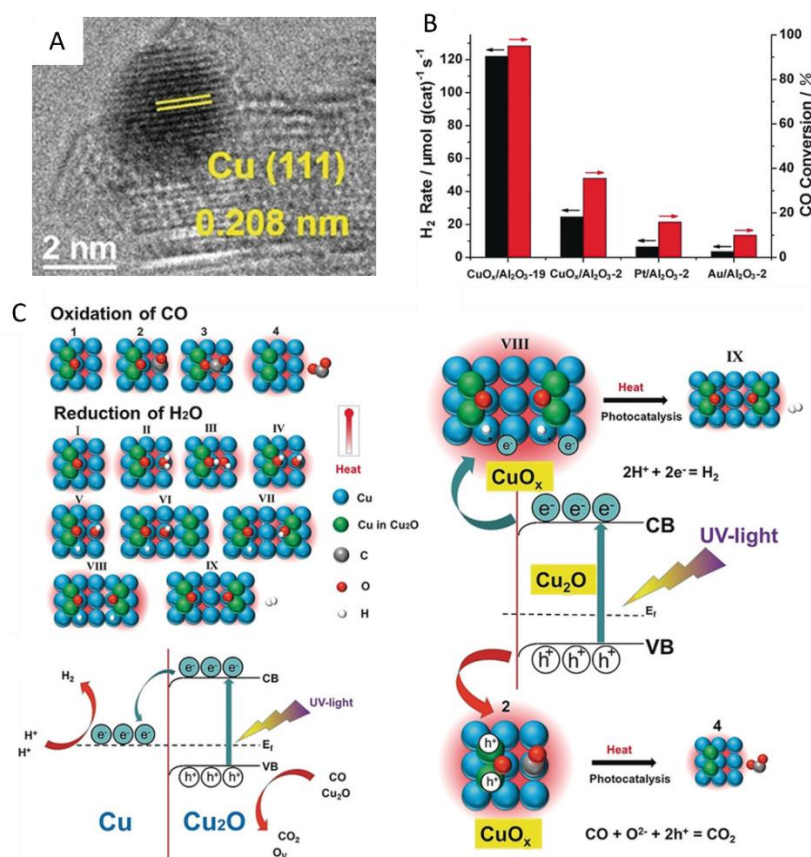


Figure 6. (A) HAADF-TEM of the $\text{CuO}_x/\text{Al}_2\text{O}_3$ catalyst. (B) H_2 evolution rates and CO conversion of $\text{CuO}_x/\text{Al}_2\text{O}_3\text{-19}$, $\text{CuO}_x/\text{Al}_2\text{O}_3\text{-2}$, $\text{Pt}/\text{Al}_2\text{O}_3\text{-2}$, and $\text{Au}/\text{Al}_2\text{O}_3\text{-2}$ catalysts. (C) Schematic illustration of photothermocatalysis and photocatalysis of WGS reaction over CuO_x ($\text{Cu}/\text{Cu}_2\text{O}$). Reproduced with permission from [107]. Copyright 2019 Wiley.

Non-noble metals, such as Fe [111,112], Cu [113,114], Ni [115–117], and Zn, have been studied as either catalysts or dopants for noble metal catalysts [118–122]. Since Cu-based catalysts are industrially important for the WGS reaction, studies using this metal are common, in which fundamental insights into the mechanisms and pathways underlying the observed performances were not completely understood. Nevertheless, developing design strategies to obtain specific facets with improved performance is not easy

due to structural complexity. In this case, Cu_2O nanocubes, nanooctahedra, and rhombic dodecahedra, bounded mainly with {100}, {111} and {110} facets, were synthesized to obtain information on the nanocrystals' activity for low-temperature WGS reactions [123]. The authors observed that the nanocubes were the most active, while nanooctahedra were inactive. DFT calculations demonstrated that the Cu–Cu suboxide (Cu_xO , $x \geq 10$) interface of the {100} surface is the active site. Following another course usually observed in the literature, such a study mainly attributed the performance to a facet-dependent surface poisoning of the active site, due to surface formate and hydroxyl intermediates stability (consequently blocking active sites of the nanooctahedra), rather than an inherent facet-dependent activity. Formerly, the authors immobilized the nanocubes onto ZnO and obtained a high-active catalyst for the reaction [123]. One can notice that this is an incredible example of how previous knowledge of the active species structure/action mechanism allows for the obtaining of highly active catalysts. Interestingly, Li et al. also performed investigations on the mechanism of low-temperature WGS reactions [124]; however, they used copper oxide nanocrystals bounded with {100}, {111} and {211} facets. They showed that nanocrystals bounded by {211} were found to be the most stable surface for Cu sites; once d-band center values, which lead to the augmented adsorption strength of CO and H_2O adsorbates when these values increase, shows the tendency $\{211\} > \{100\} > \{111\}$ facets. Although DFT studies showed that the carboxyl path is the most favorable mechanism over the three copper oxide surfaces, with H_2O dissociation as the rate-determining step, the decrease in the coordination number causes a gradual surface energy decrease, illustrating the {211} facet as the most stable surface; consequently, it is the best catalyst. Once again, such a type of study puts forward the rational design of active Cu-based catalysts for the reaction.

We have shown that associating active metal species with CeO_2 support is interesting for methane and ethanol reforming; for the WGS reaction, the same can be said. For example, Lykaki et al. prepared $\text{CuO}_x/\text{CeO}_2$ binary oxides to study nanopolyhedra, nanocubes, and nanorods' effects on the reaction. According to their findings, the nanorods showed higher reducibility, oxygen vacancies, and mobility of oxygen species, affecting the interaction among copper and ceria metals and their redox cycles. Following these conclusions, the nanorods presented the best activity, reaching the thermodynamic equilibrium conversion at 350°C [125]. When hydrothermally prepared CeO_2 nanooctahedra, nanocubes, and nanorods were used as support for Cu, the trend was different from the one observed for the binary oxides [113]. In this case, the CeO_2 nanooctahedra was the best support for the catalyst preparation, leading to the highest Cu dispersion, SMSI, and a higher amount of copper oxide relative to their CeO_2 counterparts; they also reached the highest CO conversion (91.3% at 300°C). The authors also discussed that mono and poly coordinated carbonates were probably the reaction intermediates at low temperatures, supported by DRIFTS spectra.

Interestingly, alloying Cu with Pt can also be an excellent strategy to achieve H_2 production with high purity [111]. The combination of PtCu in a bimetallic catalyst allowed the electrochemical water–gas shift process at room temperature, with a faradaic efficiency of approximately 100%. The water was reduced to H_2 at the cathode, and the CO was oxidized at the anode. The material has achieved a twelve-fold enhancement in the current density ($70.0\text{ mA}\cdot\text{cm}^{-2}$) at 0.6 V compared to a commercial Pt/C catalyst and remained stable for more than 475 h. The superior activity of the alloy catalysts was rationalized as an effect of the lower probability of electron transition from the core level to the 5d bands of Pt. The phenomena may be caused due to the partial filling of the 5d bands of Pt by the electrons transferred from Cu, reducing the amount of empty 5d states and lowering the d-band center of Pt atoms. As a result, a weakening of the CO adsorption on the Pt atoms occurs. Furthermore, the literature gives more examples of alloying Cu with Pt to lead to an improved WGS catalyst. Temperature-programmed desorption and DFT revealed that the Cu/Pt catalyst binds CO more weakly than a counterpart Pt catalyst, resulting in a considerable reduction in CO poisoning of the Cu/Pt surface compared to

Pt. Additionally, DFT calculations have demonstrated that water can be easily activated by the alloyed catalyst and, at the same time, interact with the products of that reaction and formate intermediates relatively weakly, thus, preventing poisoning of the catalyst surface [126].

Although the commercial catalysts are non-noble, the last example presented a successful catalyst using a noble metal. Thus, due to their endurance against corrosion and oxidation, noble metals have also been extensively explored for WGS applications and proved to be promising [127]. The catalyst activity of metals, including Pt [128–131], Rh [132,133], Ir [101], Au [134–137], Pd [119], and Ag, has demonstrated to be strongly dependent on many variables, such as the method for catalyst preparation, physical-chemical parameters (such as shape, size, composition), metal loading, nature of the support and, presence of promoters. [138–141]. In this context, the support can play a crucial role in the WGS reaction catalyzed by Pt NPs. At 240 °C, a 4% Pt/Mo₂C catalyst (Figure 7A) exhibited a reaction rate of 227 $\mu\text{mol/g}_{\text{cat}}\cdot\text{s}$. Interestingly, under the same conditions, a rate of 54 $\mu\text{mol/g}_{\text{cat}}\cdot\text{s}$ was measured for a commercial Cu–Zn–Al WGS catalyst, suggesting that high rates for the Pt supported on molybdenum carbide (Mo₂C) were disclosed to be related to a high density of active sites at the perimeter of the Pt particles (Figure 7B,C) [142]. Here, it is possible to conclude that not just the metal choice was essential, but also the support. The geometric effects were also significant regarding the importance of particle perimeter.

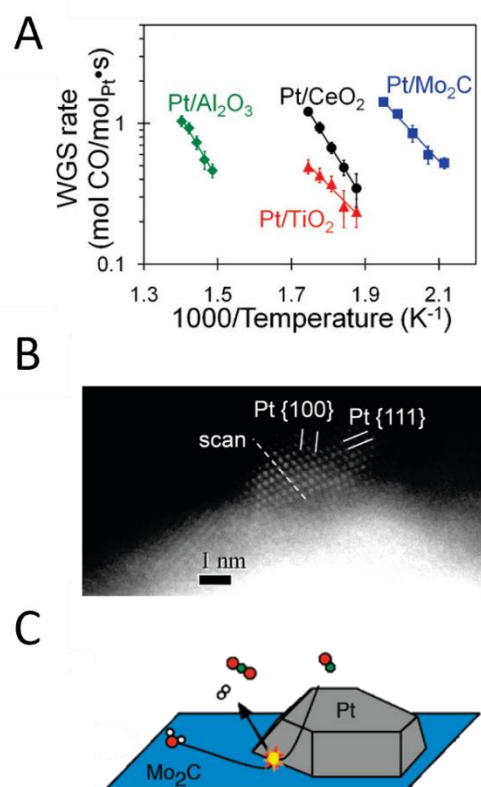


Figure 7. (A) Arrhenius plots of the WGS reaction rates for 2.7% Pt/Al₂O₃, 5% Pt/CeO₂, 2% Pt/TiO₂, and 4% Pt/Mo₂C catalysts. (B) High-resolution HAADF-STEM electron image of Pt NPs supported on Mo₂C. (C) Illustrative representation of the active sites for the WGS reaction. Reprinted with permission from [142], Copyright 2011 American Chemical Society.

Flytzani-Stephanopoulos et al.'s pioneering work disclosed the support shape's effect on the WGS reaction (Figure 8) [143]. The activity of Au NPs supported on CeO₂ nanorods (with {110} and {100} planes), nanocubes (with {100} planes), and polyhedra (with {111} and {100} planes) was shown to be strongly dependent on the shape of inorganic support. The Au/CeO₂ nanorod catalyst was the most active catalyst, followed by Au/CeO₂ polyhedra

and Au/CeO₂ nanocubes. This effect is related to a higher fraction of strongly bound gold species on the CeO₂ nanorods and polyhedral [144]. There are also studies that compare the effect of the catalyst preparation approach and CeO₂ nanostructure morphology on the catalytic activity of Pt/CeO₂ catalysts for the WGS reaction. By preparing CeO₂ nanorods and nanocubes and impregnating Pt NPs using the incipient wetness impregnation technique or strong electrostatic adsorption, the authors observed that nanocube-based catalysts, regardless of the preparation method, were more active than their nanorods counterparts. They attributed such findings to the best Pt⁰ dispersion and higher oxygen vacancies over the nanocubes; they also found out that the incipient wetness impregnation method promoted SMSI on both the support shapes [145]. A recent work by Li et al. showed the complexity of the structural evolution of the Pt/CeO₂ with multiple Pt states, its heterogeneity, and the dynamic behavior of atoms at the surface [146]. They discussed the importance of the perimeter Pt⁰-O vacancy-Ce³⁺ site for the CO oxidation in the WGS reaction and the changing in the bonding environment at the interface in which H atoms are stored with intraparticle distortion. The authors did not associate the findings with any particular CeO₂ shape in this study, showing how a deep understanding of the morphology-controlled systems is still needed.

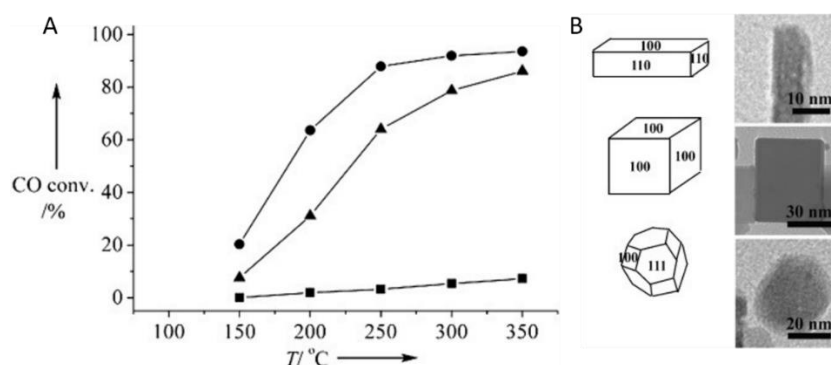


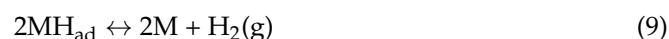
Figure 8. (A) WGS reaction profiles for 1 % Au on CeO₂ nanorods (●), -cubes (■), and -polyhedra (▲) and (B) TEM images of CeO₂ nanorods, -cubes, and -polyhedra. Reproduced with permission from [143]. Copyright 2008 Wiley.

It is important to note that the WGS reaction is classically employed to adjust the hydrogen/carbon monoxide ratio in the stream rich in H₂ from reforming, in which CO concentration can be reduced to less than 5% (v/v) at the end of the WGS process. Reducing the amount of CO in H₂ currents is crucial to several chemical processes (such as ammonia synthesis), as CO is poisonous to several noble metal-based catalysts, leading to deactivation processes [147]. The reason is Pt anode poisoning, which requires a hydrogen stream containing less than 100 ppm of CO, and, typically, this level is reached by PrOX [148]. Although discussing the PrOX reaction is far beyond our aim in this review, it is important to reference it. Thus, several catalysts have been revealed to perform the PrOX reaction, such as gold-based catalysts [149]. However, although Au-based catalysts have had remarkable improvements up to the present day, as recent reviews have shown [150,151], deactivation is a significant issue. Hernández et al. tried to address the reason for this phenomenon for an Au/CeO₂ catalyst by in-situ UV-Vis diffuse reflectance spectroscopy. They found out that the performance loss is related to the fast reduction of Au species and changes in the redox properties of ceria [152]. Non-noble metals have also been in the spotlight lately. For instance, Liu et al. prepared a CuO-CeO₂ catalyst (calcined at 650 °C, ~5 at.% Cu content) by urea gelation/co-precipitation to study PrOX of CO in an H₂ stream. They obtained 99% CO conversion and 65% selectivity at 165 °C, which is a good result [153]. Thus, as discussed before for other systems, much work has to be done to state all the related parameters necessary to improve catalytic and selectivity in the reaction.

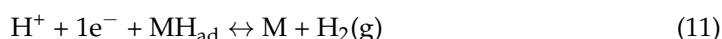
7. Water Electrolysis

Water electrolysis or electrochemical water-splitting reaction is the process whereby chemical-grade H_2 (and O_2) is obtained through the application of electrical energy [3]. Although the technique has been known for around 200 years, it only contributes to a minor segment of the total H_2 production worldwide, which opens up developments [154]. The method requires 1.23 V (vs. normal hydrogen electrode, NHE, at 25 °C and 1 atm) of thermodynamic potential, both in alkaline and acidic media, and comprises the hydrogen evolution reaction (HER) and the oxygen evolution reaction (OER) [155]. Herein, the process is mainly designed as HER, since that is the process we are interested in, but water electrolysis, in general, is also used. The most accepted mechanisms of HER for acidic, alkaline, and neutral media differ in the desorption step (other differences are also discussed in the literature in detail [156–158]) and are as follows:

Volmer–Tafel mechanism



Volmer–Heyrovsky mechanism



where H_{ad} means a surface ad-atom, and M is a surface metal site.

Electrolyzers are crucial apparatus to produce H_2 through electrolysis. However, their power supply (electricity) must come from renewable sources to be efficient and green when we consider the whole process towards a hydrogen economy [159,160]. In addition, catalysts are an essential part of the process in an energetic context, since they play a significant role in overcoming the kinetic energy barriers for electrochemical reactions in electrolysis [161]. Indeed, in a similar way to many other electrochemical processes, an overpotential (potential difference between the required and thermodynamic values) is required for H_2 production; thus, catalysts are needed to reduce such overpotential [162]. From a physical chemistry perspective, a suitable catalyst for HER needs to present low activation energy for H desorption and optimum Gibbs free energy of metal-hydrogen binding (ΔG_H^*) and H_2 desorption. Platinum-group metals have been considered the most efficient catalysts for HER since they present these features and are capable of providing high exchange current density (j_0) [163]. However, their high cost restricts their broad and industrial applications; thus, reducing their loading or replacing them with low-cost non-noble metals is essential in a hydrogen economy. Furthermore, nanotechnology tools have been used to develop advanced nanomaterials.

Volcano-type plots, which associate j_0 values with ΔG_H^* , conventionalized by Pearson in 1958 for HER, have been used so far [164]. However, Sabatier's principle dictated volcano curves for catalytic hydrogenation and dehydrogenation long before, in 1911, with plots of the reaction rate versus the free energy of adsorption of the intermediate [165]. When positive (endergonic) energy of adsorption is considered, the adsorption is not strong enough, which leads to an exponential increase in j_0 ; the opposite is true. When negative (exergonic) energy of adsorption is studied, an exponential decrease in j_0 is observed. Near $\Delta G_{ad} \approx 0$, the rate reaches a maximum [164]. Figure 9A shows the volcano-type trend between ΔG_H^* values and the measured j_0 . [166]. Although some differences are observed in the literature when the correlation considers DFT-derived ΔG_H^* [167], due to the different heat adsorption energy that the Pt facet can hold (Figure 9B), it is noteworthy that Pt is close to the apex, showing its remarkable catalytic performance toward HER. According to the plot, we have chosen some metals to discuss, emphasizing nanoscience tools for the improvement of their catalytic properties, since their general utilization is

exhaustively addressed in the recent literature [168,169]. Thus, here we discussed Pt, Pd, and Ni metals, according to controlled synthesis approaches.

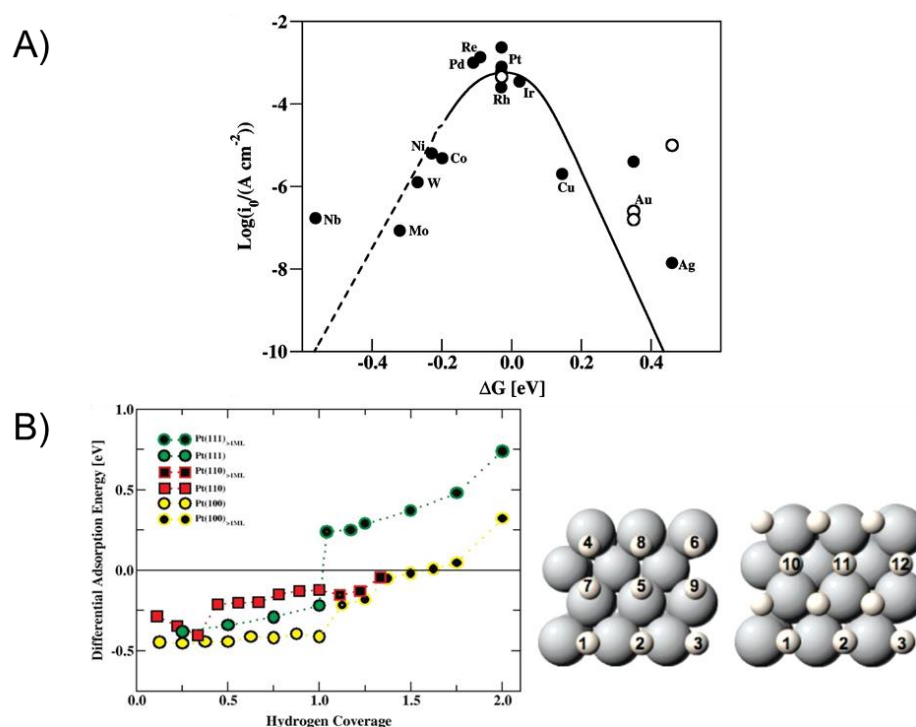


Figure 9. (A) The volcano-like plot shows the measured exchange current density vs. the calculated free energy of hydrogen adsorption at equilibrium (vs. NHE at standard conditions). (B) Differential energy of hydrogen adsorption as a function of hydrogen coverage for (111), (110), and (100) Pt facets. Reprinted with permission from [167], Copyright 2010 American Chemical Society.

Selected Metal-Based HER Electrocatalysts

Platinum: According to the volcano-type plot, platinum-group metals are expected to present remarkable performances toward HER. It is also worth mentioning that it is valid over a broad pH range [170,171]. As discussed, Pt has demonstrated the most desired capabilities required to be applied as efficient electrocatalysts for HER; thus, recent reviews have dealt with the properties of this metal [158,172]. Accordingly, its properties are now being improved by rationally designing and engineering active crystalline facets of the metal NPs [173]. Although such a strategy is not new since Markovic et al. have indicated the different activities toward HER due to Pt facets, following the order $\text{Pt}\{110\} > \text{Pt}\{100\} > \text{Pt}\{111\}$ [174], obtaining well-defined facets of noble metals is not always easy, but the use of sacrificial templates can aid such methodology [173,175]. However, we believe that more efforts in engineering facets are still missing in the literature to achieve improved HER performances.

Zhao et al. successfully obtained PtNi-O/C octahedra nanostructures with $\text{Ni}(\text{OH})_2$ -Pt(111)-like interfaces on its surface by annealing PtNi/C structures (Figure 10). The PtNi-O/C material presented a mass activity of $7.23 \text{ mA}/\mu\text{g}$ at an overpotential of 70 mV, which is almost 8 times higher than the performance of the commercial Pt/C catalyst [176]. Zhang et al. also showed how a controlled synthesis could influence the electrocatalytic activity and stability of a catalyst toward the HER under alkaline conditions. By synthesizing well-crystalline lotus-thalamus-shaped Pt-Ni anisotropic superstructures via a solvothermal approach, they obtained an overpotential of 27.7 mV at a current density of 10 mA cm^{-2} and a turnover frequency of $18.63 \text{ H}_2 \text{ s}^{-1}$ at an overpotential of 50 mV [177]. Interestingly, Koo et al. prepared Pt nanocubes of different sizes using alkyltrimethyl-ammonium bromide, K_2PtCl_4 , and NaBH_4 by changing the chain lengths of the surfactant and their

concentration. The Pt nanocubes (8, 20, and 25 nm) were coated on fluorine-doped tin oxide (FTO)/glass substrate by drop-casting and evaluated. The authors, under optimized conditions, obtained 1.77 A mg^{-1} at an overpotential of 50 mV and 0.54 A mg^{-1} at 100 mV with the intermediate size nanocubes, which were bounded by {100} facets, with some corners cut exposing {110} facets. However, they found that not only nanocubes were formed (cuboctahedra were also observed in the images) [178]. Thus, it is clear that the shape effect plays a critical role in catalytic performance. However, the size is also essential and has been thoroughly discussed in the catalysis field [179,180]. What if SAs are obtained? Would they be active for HER? The literature suggests a resounding yes.

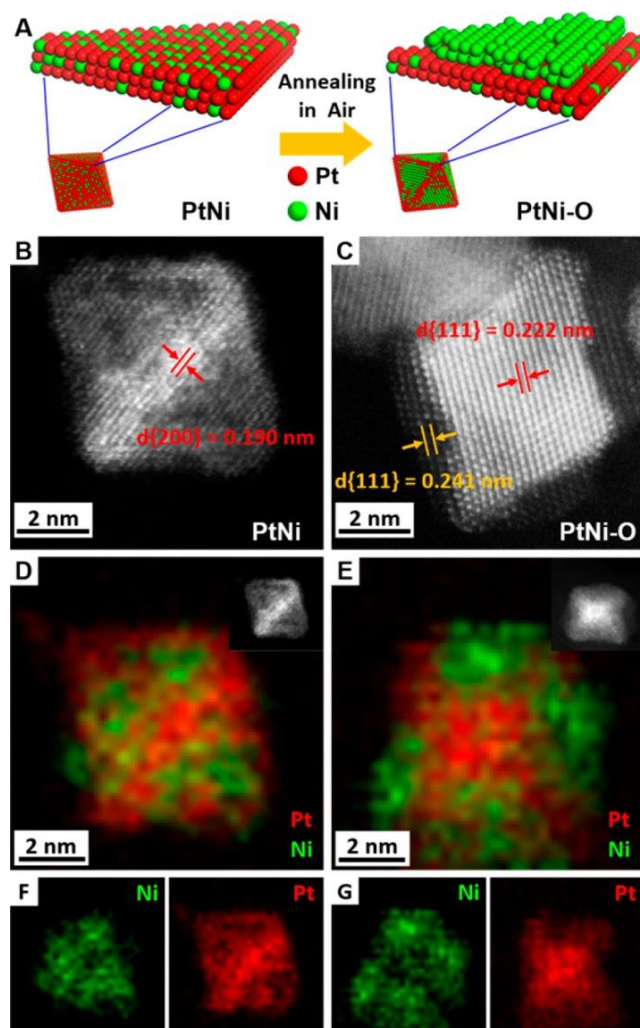


Figure 10. (A) Annealing process scheme of PtNi/C being converted to PtNi-O/C. (B) PtNi/C and (C) PtNi-O/C HAADF STEM images showing their octahedral structure. EDX maps of the (D) PtNi/C (E) PtNi-O/C octahedral NPs. (F) EDX maps of Ni and Pt in D. (G) EDX maps of Ni and Pt in (E). Reprinted with permission from [176], Copyright 2018 American Chemical Society.

Interestingly, Zhang et al. proposed an electrochemical deposition approach to immobilize Pt SAs over nanosheets of a two-dimensional inorganic compound ($\text{MXene-Mo}_2\text{TiC}_2\text{T}_x$), in which Mo vacancies were essential for the immobilization of Pt atoms. The authors attributed the strong covalent interactions between the Pt SAs and the support to the high catalytic ability for HER of the catalyst, with low overpotentials of 30 and 77 mV to achieve 10 and 100 mA cm^{-2} , respectively. Such a process maintained individual atoms, avoiding the formation of aggregated particles. Moreover, the material showed almost 40 times more mass activity than a regular Pt/C catalyst [181]. Following another efficient strategy for

preparation and preservation of Pt SAs, Yu and collaborators promoted a chemical bind of 2,6:2',2''-terpyridine onto a 3D carbon support in a single step and, later, submerged the material in a vial containing an aqueous $K_2[PtCl_4]$ solution with an available concentration of 0.5 ppm Pt^{2+} , for 2 h at room temperature for the Pt SAs obtaining. This process allowed them to reach a very low metal loading ($0.26 \pm 0.02 \mu g \cdot cm^{-2}$ of Pt) with a mass activity of $77.1 A \cdot mg_{Pt}^{-1}$ at 50 mV, which is a very high accomplishment [182]. In addition, using a metal-selective ligands method, Elmas et al. synthesized an electropolymerizable monomer (4-(terthiophenyl)-terpyridin) with a pendant terpyridine unit, which was found to be selective for platinum-group metal complexation. The resulting metallopolymer exhibited Pt SAs that were able to catalyze HER under different conditions and configurations with remarkable activity [183].

Other exciting examples are available in the literature. For example, Cheng et al. prepared Pt SAs and clusters over nitrogen-doped graphene nanosheets by an atomic layer deposition technique for HER and proposed that almost all the Pt atoms in the system were in use, which is engaging from an economic perspective. The catalyst exhibited 37 times more activity than the commercial Pt/C catalyst [184]. Sun et al. also used the atomic layer deposition technique for Pt SA immobilization on graphene nanosheets without doping of the support; however, in this case, their catalytic process was 10 times more active than the commercial Pt/C catalyst [185]. Thus, in the SAs' case (and usually in many other nanostructures systems), the support is crucial once the atoms are impregnated onto its surface. Consequently, the support choice is essential, and the metal-support interaction (MSI) is also important to tune the electronic structure and reactivity. For example, Shi et al. obtained Pt SAs by a site-specific electrodeposition technique over two-dimensional transition metal dichalcogenides supports (MoS_2 , WS_2 , $MoSe_2$, and WSe_2). Their studies provide further understanding of the MSI importance. They found that the anchoring chalcogen (S, Se) and the transition metal (Mo, W) can synergistically modulate the electronic structure of Pt SAs by tuning the d-orbital state of the metal. This regulation achieved by MSI prompts the alkaline and acidic HER due to the optimization of hydrogen adsorption, which speeds up reaction kinetics for water dissociation. Among the samples, the best mass activity was achieved for Pt SAs over $MoSe_2$, $34.4 A \cdot mg^{-1}$ under an overpotential of 100 mV [186]. One can notice that, although incredible achievements are discussed, wet-chemical syntheses tend to be chosen due to their more straightforward process [187,188].

Therefore, the way the SAs' catalysts act is still a challenge, and as the support influences it, no generalizations are possible. However, Fang et al. provided *operando* synchrotron X-ray absorption spectroscopy/theoretical simulations that evidenced that Pt SAs over an N-C framework present a structure less coordinated to the support at quasi zero-valence during the reaction conditions, with 5d density as the real active centers [189]. Indeed, it is just an isolated example, and more theoretical simulations are needed to understand the catalytic systems better. Recent literature is available for more information on Pt SA systems [168,169,172]. It is important to mention that the SA syntheses methods cited here are applicable for catalyst syntheses that match the other technologies described; also, similar conditions are used to obtain SAs of different metals.

Palladium: The Pd's atomic size has shown to be comparable to Pt's, making it suitable as an alternative catalyst for HER [164]. Moreover, Pd is cheaper, and several efficient synthetic strategies have been reported, allowing both size- and shape-controlled synthesis of Pd nanocrystals [190–192]. For example, Pd nanooctahedra bounded by (111) facets (with an average tip-to-tip size of 7.8 nm and narrow size distribution) presented a very high H loading of 0.90, which can be interesting for HER applications [193]. In this context, Li et al. designed a core@shell PdCu@Pd nanocube catalyst for highly efficient HER. First, they prepared PdCu nanocubes by co-reduction of $Cu(acac)_2$ ($acac$ = acetylacetonate) and Na_2PdCl_4 in the presence of oleylamine and trioctylphosphine, then covered the cubes with Pd using anodization at a constant potential of 0.51 V vs. Ag/AgCl at room temperature in 0.5 M H_2SO_4 solution for 10 s. HAADF-STEM and EDX elemental mapping images showed that the synthesis was efficient (Figure 11). The system required an overpotential of 10 mV

to reach a current density of 68 mA cm^{-2} [194]. Wang et al. prepared Pd icosahedral NPs with a lattice spacing of 0.22 nm, ascribed to the (111) plane, using a polyol method that counts polyvinylpyrrolidone as a stabilizer. The optimum catalytic activity, which is better than the obtained for the commercial Pt/C, was achieved after 130,000 cyclic voltammetric cycles, with an overpotential of 32 mV at 10 mA cm^{-2} , indicating its high durability and activity [195]. The same here was felt for Pt NPs; not much literature with controlled Pd NPs is available for HER applications.

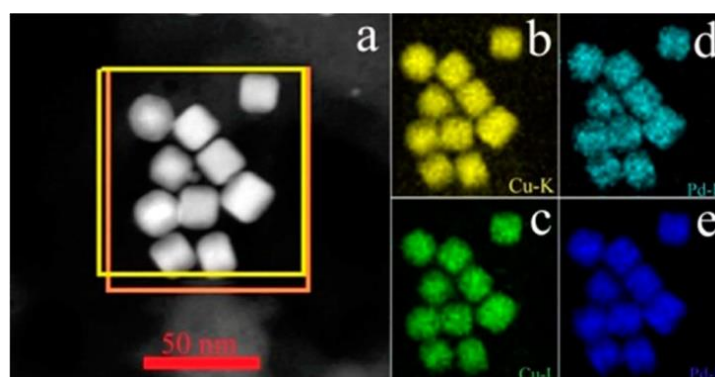


Figure 11. (a) HAADF-STEM image of the PdCu@Pd nanocubes. HAADFSTEM-EDX elemental mapping images of (b) Cu-K, (c) Cu-L, (d) Pd-K, and (e) Pd-L. Reprinted with permission from [194], Copyright 2017 American Chemical Society.

Nickel: Ni has been considered a good alternative non-noble metal candidate for HER, since it holds similar chemical properties and has the same group number of Pt. In addition, it is cheaper and more abundant relative to both Pt and Pd. In alkaline conditions, a previous report claimed that the rate-determining step is the adsorption of hydrogen (Volmer step) and that HER can be improved in the presence of the low-valence-state oxide of Ni [196]. A recent review discussed that Ni-Pt and Ni-Mo alloys are interesting for the reaction, also highlighting that Ni-nitride, -oxide, -phosphide, and -sulfide-based catalysts (among other examples) may work as bifunctional catalysts for both hydrogen and oxygen evolution reactions [197]. An interesting study was published by Li et al. using a Cu-Ni alloy. They obtained edge-notched Cu@Ni nanocubes, edge-cut Cu@Ni nanocubes, and mesoporous Cu-Ni nanocages by a selective wet chemical etching method (Figure 12). Interestingly, the two last materials were etched to produce the highly catalytically active (111) facets. However, the Cu-Ni nanocages were the nanostructures that showed higher activity for HER under alkaline conditions (current density of 10 mA cm^{-2} in an overpotential of 140 mV). Moreover, the authors revealed by density functional theory that the Ni-Cu alloys are more active than pure Ni, since it presents too strong adsorption energy of the intermediate state (adsorbed H^*), hampering the reaction [198]. Nanocubes of Ni(OH)_2 and Ni-Fe modified with Pt atoms were also proposed in the literature for the reaction, promoting the reduction of the noble metal loading [199,200]. Following such a process of alloying with Pt, Kaviani et al. synthesized Pt-Ni octahedral nanocrystals of 9 nm in size that showed 15-fold enhancement in specific activity and almost 5 times more mass activity in an alkaline media, when compared to the Pt/C commercial catalyst [201]. Seo et al. showed that spherical nickel phosphide nanocrystals bounded by (001) facets surface showed higher HER activity than rod-shaped nickel phosphide nanocrystals bounded by (210) facets considering overpotential, Tafel slope, and turnover frequency [202]. Nickel phosphide nanowires were also prepared by Xiang et al. via a one-step hydrothermal approach with an overpotential of 320 mV and a Tafel slope of 73 mV dec^{-1} for HER [203].

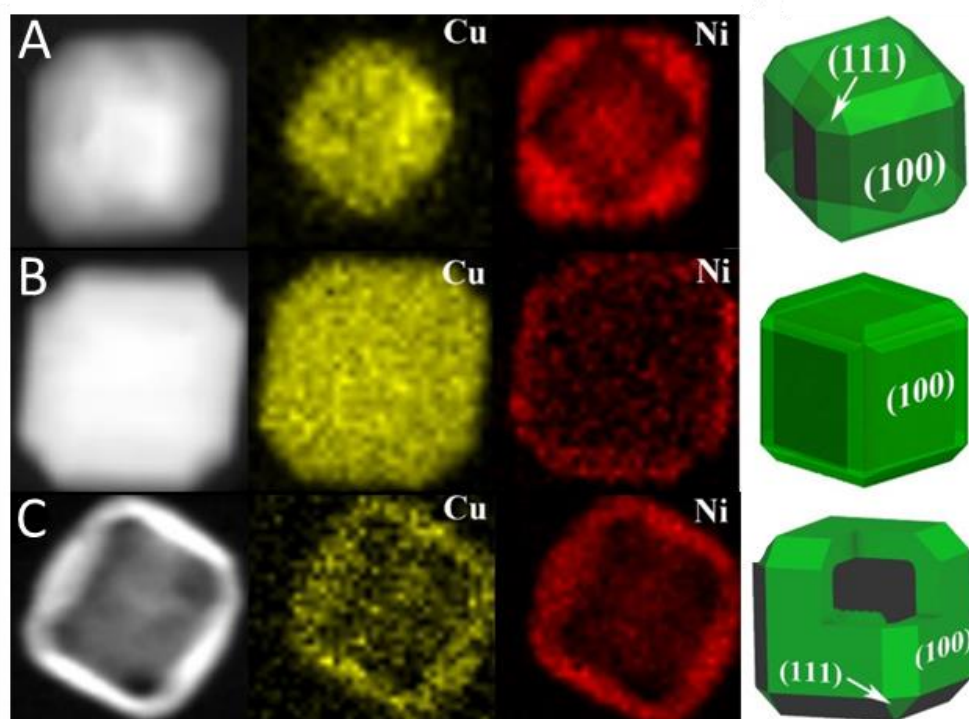


Figure 12. EDX elemental mappings and schematic representation of (A) edge-cut Cu@Ni nanocubes, (B) edge-notched Cu@Ni nanocubes, and (C) Cu–Ni nanocages. Reprinted with permission from [200], Copyright 2019 American Chemical Society.

8. Photochemical Water-Splitting Reaction

Developing low-cost, efficient, and stable technologies for converting light into chemical energy can be a promising approach to circumventing both energy and environmental problems. One of these clean strategies for H_2 production is photocatalytic water splitting, a thermodynamically uphill transformation associated with positive Gibbs free energy ($237 \text{ kJ} \cdot \text{mol}^{-1}$ or 1.23 eV) [204]. Generally, the process has three main steps, which are as follows: (1) light-harvesting with charge carriers generation (negative electrons in the conduction band (CB) and positive holes in the valence band (VB)); (2) charge immigration, transfer, and separation; and (3) initiation of the redox reaction on the photocatalyst surface. In the last step, electrons act as reducing agents to transform water into hydrogen, and holes act as oxidizing agents to produce oxygen from water [205]. Therefore, the bandgap energy (E_g) should be in an energy range of $3.0 \text{ eV} > E_g > 1.23 \text{ eV}$ to efficiently use solar energy [206]. The photocatalyst's band position (VB and CB) should be located appropriately to accomplish the water-splitting reaction. Thus, the CB lowest energy level must be more negative than the hydrogen evolution potential (EH_2/H_2O , 0 V vs. NHE), and the VB highest energy level must be more positive than the oxygen evolution potential (EO_2/H_2O , 1.23 V vs. NHE) [207]. Other factors, such as pH, charge transfer and separation, charge recombination, and light intensity, greatly influence the efficiency of H_2 production via water splitting [208].

Since the pioneer paper reported by Fujishima and Honda on the photodecomposition of water in the presence of Pt and TiO_2 electrodes under UV light [209], tremendous efforts have been directed to the development of efficient semiconductors, such as metal oxides, carbon-nitrides, polymers, and heterostructures, to produce H_2 under light irradiation [210]. Usually, an n-type/p-type semiconductor can act as a photoanode/photocathode, respectively. N-type and p-type semiconductors are created by doping intrinsic semiconductors with an electron donor or electron acceptor element, respectively; p,n-type semiconductors are made when n- and p-type dopants are merged to create a semiconductor [204,211]. Thus, strategies have been made to increase the charge separation efficiency of photocatalysts

using semiconductor engineering. However, oxide photocatalysts show inferior performance without a cocatalyst, which is a noble metal or another transition metal oxide that decorates the support surface [212] and prompts advanced strategies for catalyst syntheses.

Currently, H_2 production by photocatalytic water splitting has some critical unsolved problems, such as low catalyst stability and efficiency and high cost [213]. In this view, heterostructure formation has been widely adopted as an efficient strategy to overcome such drawbacks, since hybridization between two or more transition metal-based materials synergistically enhances their performance. Thus, it is possible to choose an active material for HER that can be combined with another active material for OER [214–217]. By preparing this review, we believe that heterojunctions are one of the most motivating fields for photochemical water-splitting issues, due to their synergetic multi-component characteristics [218]. The enhancement is evidenced by a recent study published by Sitara et al. They prepared heterostructures comprised of MoS_2 and $CoTe$ by a hydrothermal method/ultrasound with different wt.% ratios. The material $MoS_2/CoTe$ (1:1) reached a maximum photocurrent density of 2.791 mA/cm^2 , which was found to be about 11 times higher than the pristine MoS_2 under a light intensity of 100 mW/cm^2 [219]. Shit et al. also showed the enhancement of electrocatalytic activity by heterostructures of cobalt sulfide/nickel sulfide heterostructures supported by nickel foam, which facilitated charge transport for a synergistic effect toward HER and OER in an alkaline medium [216].

Continuing our analysis of heterojunctions, the conductivity can be remarkably improved by coupling active species with conductive supports. For example, by a hydrothermal route, Lucas et al. prepared photoanodes comprising TiO_2 nanotubes and lanthanum-doped $SrTiO_3$. They used this catalyst for the photoelectrochemical split of water under simulated solar irradiation. The process led to a photocurrent density of $109.4\text{ }\mu\text{A cm}^{-2}$ (at 1.23 V vs. RHE). Doping the $SrTiO_3$ overlayer with 10 mol% of La^{3+} enhanced the photoelectrochemical response to $144.2\text{ }\mu\text{A cm}^{-2}$ (1.23 V vs. RHE) [220]. Similarly, Ni_3N was used as an active cocatalyst onto $g-C_3N_4$ by Ge et al. They obtained H_2 production under visible-light irradiation with a hydrogen evolution rate of $\sim 305.4\text{ }\mu\text{mol h}^{-1}\text{ g}^{-1}$, which is about three times higher than that of pristine $g-C_3N_4$ [221]. Ni_3C NPs were used as cocatalysts to modify CdS nanosheets (OD vs. 2D materials). Under visible light irradiation, the authors obtained H_2 production rates of $357\text{ }\mu\text{mol h}^{-1}$ in $0.25\text{ M Na}_2\text{S-Na}_2\text{SO}_3$ and $450.5\text{ }\mu\text{mol h}^{-1}$ in lactic acid, which were almost 8 and 5 times higher than that observed for the CdS nanosheets [222]. In this context, Ni-based photocatalytic H_2 production cocatalysts are part of the strategies to enhance further the activity and stability of photocatalysts [223]. For instance, Ag NPs were impregnated on the surface of $g-C_3N_4$ by an in-situ calcination method, before loading NiS onto the structures by a hydrothermal method. Under solar-light irradiation, an H_2 production rate of $9.728\text{ mmol}\cdot\text{g}^{-1}\cdot\text{h}^{-1}$ was obtained, which is almost 11 times higher than that achieved by pure $g-C_3N_4$ [224].

Although the H_2 production with the n-type TiO_2 semiconductor electrode has been known for a long time [225], efforts in the literature to improve this material are notorious. Based on this, Chandra et al. recently prepared hierarchical urchin-like TiO_2 with 1D nanorods as subunits via a surfactant-free solvothermal route, which showed higher photocatalytic performance when compared to NPs (H_2 evolution of 5753 mmol g^{-1}). In the study, they were able to tune anatase–rutile mixed-phases by controlling the ratio of water and HCl used, in which acid was influential in the formation of the nanorods; the performance was attributed to an efficient mechanism of charge separation in the interface of the TiO_2 phases [226]. Even though that is a great example, up to date, no material has achieved an industrial level for producing H_2 through this reaction, since the performances are still insufficient. Therefore, noble metal-based materials, such as Pt, Ir, and Ru, and non-noble metals, such as Cu, Bi, Al, Ni, Co, and Fe (among others), are considered efficient electrocatalysts for the water-splitting reaction [227–230]. In addition, alloys are essential for the field. Li et al. used an alloying approach for photochemical water splitting. In this case, they prepared Ti-Ni-Si-O nanostructures on Ti–1Ni–5Si alloy foils via electrochemical anodization, obtaining under optimized conditions a photocurrent density of

0.45 mA/cm² at 0 V (vs. Ag/AgCl) in 1 M KOH solution [231]. Studies on the preparation of Pt alloys supported under low noble metal loadings at the semiconductors' surface are also considered.

Hence, developing new or improving photocatalytic systems is highly required in a hydrogen economy context. From this perspective, it is expected that the use of nanotechnology tools will allow the design of efficient nanophotocatalysts and significantly improve the production of clean hydrogen energy [232]. The direct advantage of controlling nanomaterial synthesis (size, morphology, and composition) includes relevant improvements in catalytic performances, allowing cost reductions and singular opportunities for the maximization of activities via controlled synthesis [233–235]. Among these approaches, morphology modulation is highly discussed, as it can tune the number of active sites due to exposing specific different crystal planes, acting on the charge transfer efficiency [236–238].

Da Silva et al. recently reported the development of efficient nanocatalysts for photocatalytic water splitting, employing bimetallic PdPt NPs supported on TiO₂ nanowires with a low loading of noble metals and controlled sizes, shapes, and compositions. TiO₂ nanowires obtained by a hydrothermal method displayed well-defined shapes and uniform sizes (Figure 13A) [239]. In addition, they could be directly employed as physical templates for the nucleation and growth of Pd, Pt, and PdPt NPs over their surface without any modification/functionalization. Figure 13B–D shows typical TEM images of bimetallic PdPt-TiO₂ nanowires obtained by this approach (the inset shows EDX elemental mapping). In this case, the PdPt NP composition was controlled by manipulating the PdCl₄^{2−}/PtCl₆^{2−} molar ratios to give Pd_{0.22}Pt_{0.78}, Pd_{0.46}Pt_{0.54}, and Pd_{0.73}Pt_{0.27}-TiO₂ nanowires. While no significant conversion was detected for the pure TiO₂ nanowires, all the Pd, Pt, and PdPt nanowires displayed suitable catalytic activities at room temperature. Interestingly, they found that the highest H₂ production activity was observed over the Pd_{0.22}Pt_{0.78}-TiO₂ nanowires. The amount of H₂ produced in the third cycle was found to be 11.0 mmol/gcatalyst, which is virtually the same as what was produced in the first cycle (11.6 mmol/gcatalyst), indicating that the catalytic activities remained almost unaffected and that the successive reaction cycles did not lead to detrimental structural modifications. Their results showed that the activities correlate with the composition of the PdPt-TiO₂ nanowires, the electronic effects, and the concentration of oxygen vacancy sites at the catalyst surface, which were investigated by XPS. Figure 13E–G displays volcano plots of the H₂ yield, current density, oxygen vacancies (Os), and adsorbed water (OL) ratio (Os/OL) as a function of the PdPt composition at the surface of the TiO₂ nanowires (Pd_{0.2}Pt_{0.78}-TiO₂).

Zheng et al. elegantly prepared a high-advanced catalyst for the water-splitting reaction [240] using noble and non-noble metals in one pot. They designed a Janus photocatalyst by preparing SiO₂ spheres functionalized with APTES, which displayed terminal amino groups. Then, after Pt NP immobilization onto the spheres (Pt/SiO₂), the prepared material underwent a reaction with a mixture of TEOS and n-octadecyltrimethoxysilane (mSiO₂/Pt/SiO₂). The mSiO₂/Pt/SiO₂ material was used as the template for carbon nitride covering, promoted by sonication of cyanamide, with further stirring at 60 °C overnight; NH₄HF₂ was used to remove the silica template, leaving hollow carbon nitride spheres containing Pt NPs in its interior (designed as hollow carbon nitride spheres, HCNS/Pt). As a final step, they immobilized Co₃O₄ onto the previously prepared material—Co₃O₄/HCNS/Pt (Figure 14). Such precise modification allowed a catalyst with spatially separated oxidation and reduction centers to be obtained, decreasing charge recombination. Comparing the photocatalyst with the Pt and Co₃O₄ loaded on the inner and outer surfaces with a counterpart pursuing random distribution of Pt and Co₃O₄ only on the external surface with the same metal loading showed about 10 times faster gas evolution. More examples of this perspective are available in recent reviews [241,242].

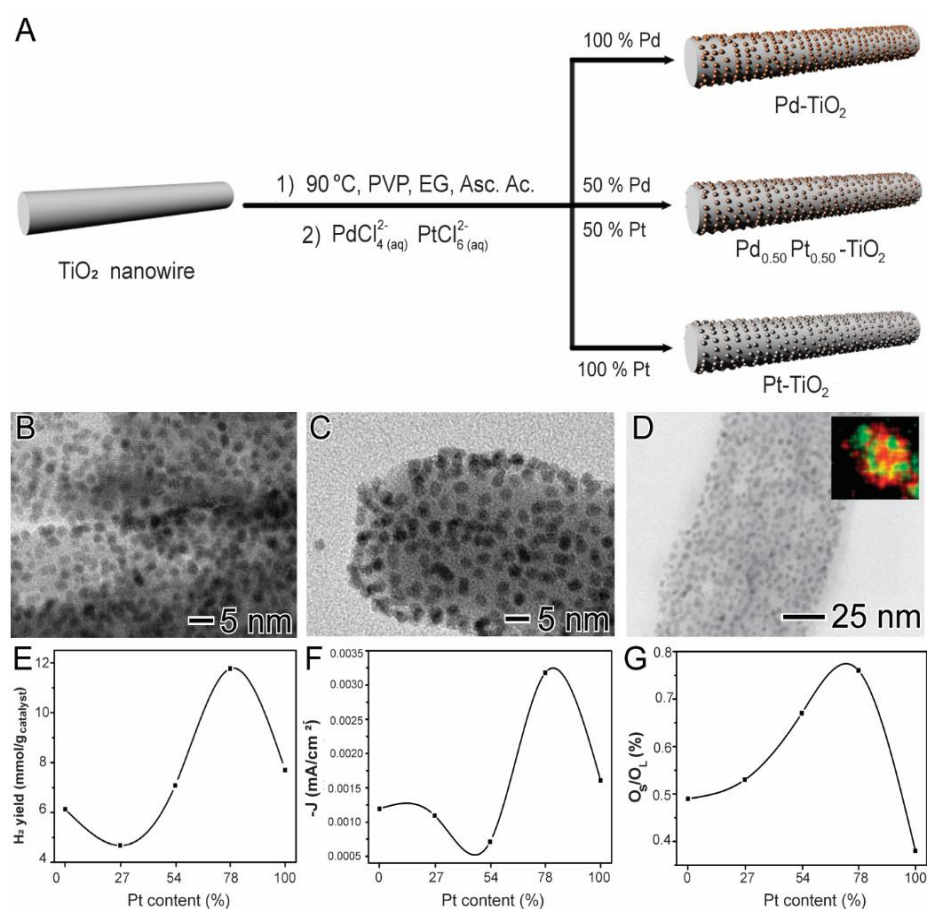


Figure 13. (A) Strategy for synthesizing TiO₂ nanowires decorated with Pd, Pt, and PdPt NPs. (B–D) HRTEM images of TiO₂ nanowires decorated with small Pd (B) Pt (C,D) Pd_{0.50}Pt_{0.50} NPs covering the entire surface of the nanowires. The inset image represents STEM-EDX elemental mapping of individual Pd (green) and Pt (red) at the surface of TiO₂ nanowires. (E) plots of H₂ yield (F) current density and (G) Os/OL ratio as a function of PdPt composition. The volcano-type relationships were observed for Pd_{0.2}Pt_{0.78}-TiO₂ composition. Reproduced with permission from [239]. Copyright 2019 American Chemical Society.

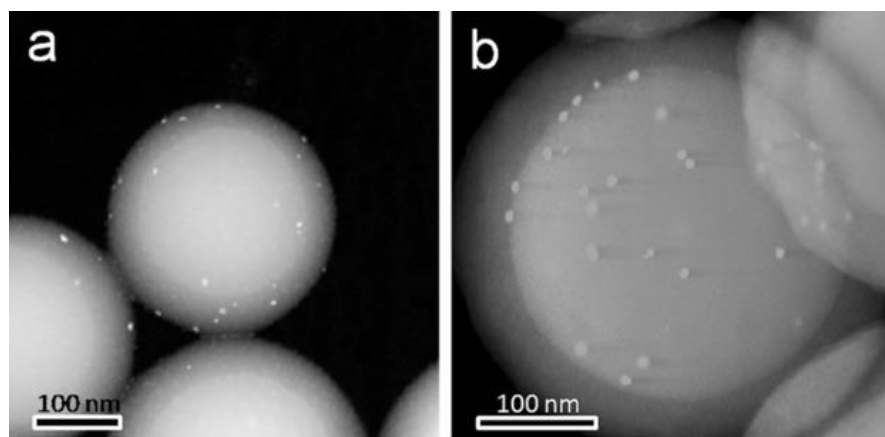


Figure 14. Cont.

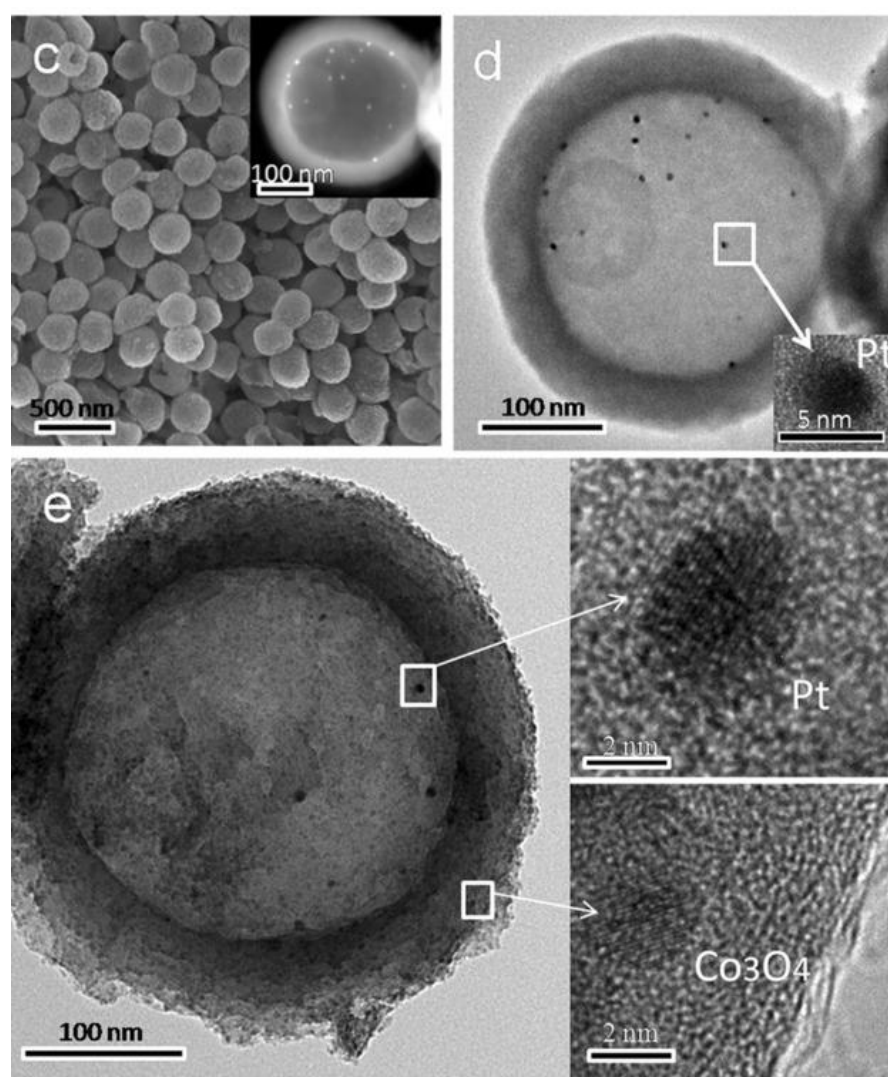


Figure 14. TEM images of (a) Pt/SiO₂ and (b) mSiO₂/Pt/SiO₂ spheres; (c) SEM and (d) TEM images of HCNS/Pt samples; (e) TEM and HRTEM images of Co₃O₄/HCNS/Pt samples. Reproduced with from [240]. Copyright 2016 Wiley.

9. Conclusions and Perspectives

The recognition of nations to avoid a climate catastrophe is undeniable. Public concerns over climate change have grown, and governments, organizations, and institutions worldwide are adopting pollution-slashing initiatives based on the Paris Agreement (2015) in an attempt to achieve net-zero emissions by 2050 (net-zero is reached when the amount of carbon added to the atmosphere is lower than the amount removed). Furthermore, global energy transition actions were discussed to be put into practice at COP26 (2021). The aim is to reduce greenhouse gases emissions without delay and keep the increase in global temperature this century at a maximum of 2 °C, or 1.5 °C ideally. Thus, the H₂ production for future widespread applications is a latent necessity, bearing in mind that the primary sources of renewable energy (solar and wind) are intermittent, and H₂ technologies can solve inconstancy issues, such as storing surplus renewables power when the grid cannot absorb it.

It is well-known that advances in synthetic and characterization approaches have facilitated a fundamental understanding of how catalysts work. This, in turn, guides their rational design and synthesis, resulting in enhanced performances to achieve the level of industrial relevance, qualified for scale-up pilot studies, and eventual commercialization [243]. Based on this, a potential cost reduction for H₂ production depends on

more efficient materials, and breakthroughs in alternative technological developments are required. In this review, we focused on nanocatalysts for different H_2 production technologies that overview how catalysts can be nanoengineered at the sub-nano or atomic scale, including shape, composition, and structure to achieve high activity, selectivity, and stability. Thus, we presented a brief overview of the main production techniques for H_2 production, focusing on nanoengineering approaches for catalysts' parameter control (shape, size, composition, structure, electronic, and support interaction) and their performance. Despite the remarkable progress in the area, we believe that material design is still in the early stages, and little is known yet regarding their application for H_2 production, which hampers widespread applications.

Herein, we presented several examples showing that metal NPs pursue a range of tunable properties that can be associated with controlled supports for improved catalysis. In this context, the following issues must be addressed: (1) fundamental understanding of the mechanisms regarding the catalyst processes is lacking, which hampers new catalyst development; (2) the interface of metal/support is complex and, up to now, poorly understood, holding back more efficient syntheses; (3) theoretical models consisting of electronic structures are required; (4) controlled synthesis regarding shape and exposition of specific facets were presented herein for some applications and were proved to be efficient; however, much efforts are needed in this field to understand such singularities and future applications; (5) supports are crucial for catalytic issues as shown, and their structural development must be mandatory. Although it is not an easy task, it would be good to understand such systems better to draw some generalizations, i.e., we have shown that some studies used similar morphologies using the same materials, but different tendencies were observed. What is behind such findings? This question shows that understanding the interactions between particular surface facets/morphologies of supports and the active species is crucial for clarifying the observed performances' mechanisms. Apart from a synthetic perspective, we need to rationalize the modifications that the materials undergo during the reaction. Thus, in-situ studies are critical to an advanced comprehension of catalytic processes and can increase the catalysts' design, aiming performance.

Water electrolysis has shown excellent possibilities for green energy savings as an energy conversion technology, and future plants are expected to contribute to the large-scale storage of renewable energy, since it is already applied at an industrial scale. In industry, alkaline electrolysis has been used for more than a century, and the main challenge for obtaining H_2 by this process is the cost, which does not match market and tax necessities [244]. Moreover, it is well-known that the electrochemical hydrogen and oxygen evolution reactions are slow in nature. Therefore, the use of electrocatalysts based on noble metals is highly needed, and, due to stability issues, the cost-performance ratio of water electrolysis is again a significant issue. This situation opens up fair advances in the technology itself and catalysts used. In addition, efforts to lower the metal loading on the process are not straightforward due to stability or performance issues and are under continuous improvement. However, all these drawbacks are being analyzed and will be overcome soon, as this process is the strongest candidate in a carbon-neutral context, prompting researchers worldwide to study it.

The generation of H_2 employing water splitting has become a key route for replacing the energy obtained by fossil fuels with solar energy. In this scenario, H_2 production by photocatalysis and photoelectrochemical cells in the presence of sunlight are potential future methods in development. Although it is still in its initial development, the photoelectrolysis process is considered a viable method, presenting low conversion efficiency up to now [204]. Thus, there is massive potential for sustainable H_2 generation developments; however, the challenges and limitations, including low H_2 yields and side reactions that convert H_2 into by-products before it is harvested, still need to be solved as they face the challenge of high production costs and increased storage requirements. Hence, much is needed to be developed and studied for photocatalytic processes concerning catalysts for the overall water-splitting reaction, including studies related to interface engineering, morphology,

and elemental doping. Furthermore, reproducible efficiencies from photocatalysis are around 1%, and at least 10% are necessary for industrial application [245].

The technologies presented herein are among the most developed/in development for H₂ production. In addition, indeed, there is room for their improvement in the next few years, specifically regarding the catalytic systems' cost, efficiency, and durability, which is the focus of the present review. Currently, non-noble catalysts are being studied for technological improvements. Furthermore, it is essential given that it is estimated that 7% of the world's platinum supply will be required for fuel cell use in Europe in 2030 [246]. Thus, to briefly summarize, all these proposals tend to improve the processes to a new level, enabling studies to move towards a design-driven approach that allows catalytic systems to be planned earlier in the process, paving the way for cleaner energy generation and sustainable progressions.

Author Contributions: Conceptualization, writing—original draft preparation, M.A.S.G.; writing—review and editing, J.L.F., R.B.d.L., M.L.G., E.C.K., M.L.Z., A.A.T., A.G.M.d.S., P.V., M.A.S.G. and G.M. All authors have read and agreed to the published version of the manuscript.

Funding: This research was funded by FAPESP through project 2015/14905-0, by FAPESP and SHELL Brazil through the 'Research Centre for Gas Innovation—RCGI' (FAPESP Project 2014/50279-4 and 2020/15230-5), hosted by the University of Sao Paulo, and the support given by ANP (Brazil's National Oil, Natural Gas, and Biofuels Agency) through the R&D levy regulation. There was also funding of the Fundação de Amparo à Pesquisa do Estado do Rio de Janeiro (FAPERJ, grant number E-26/201.315/2021), Fundação de Amparo à Pesquisa do Maranhão (FAPEMA, grant number 01372/17-UNIVERSAL), and Coordenação de Aperfeiçoamento de Pessoal de Nível Superior—Brasil (CAPES)—Finance Code 001 (CAPES Portaria No 206, de 4 de setembro de 2018). The APC was funded by the Hydrogen Journal.

Acknowledgments: The authors acknowledge FAPESP, SHELL Brazil through the 'Research Centre for Gas Innovation—RCGI, ANP, FAPERJ, FAPEMA, and CAPES.

Conflicts of Interest: The authors declare no conflict of interest.

References

- Griffiths, S.; Sovacool, B.K.; Kim, J.; Bazilian, M.; Uratani, J.M. Industrial decarbonization via hydrogen: A critical and systematic review of developments, socio-technical systems and policy options. *Energy Res. Soc. Sci.* **2021**, *80*, 102208. [CrossRef]
- Fan, L.; Tu, Z.; Chan, S.H. Recent development of hydrogen and fuel cell technologies: A review. *Energy Rep.* **2021**, *7*, 8421–8446. [CrossRef]
- McCay, M.H.; Shafiee, S. Hydrogen: An energy carrier. *Future Energy Improv. Sustain. Clean Options Our Planet* **2020**, 475–493. [CrossRef]
- Kalamaras, C.M.; Efstathiou, A.M. Hydrogen Production Technologies: Current State and Future Developments. *Conf. Pap. Sci.* **2013**, *2013*, 690627. [CrossRef]
- Kanz, O.; Bittkau, K.; Ding, K.; Rau, U.; Reinders, A. Review and Harmonization of the Life-Cycle Global Warming Impact of PV-Powered Hydrogen Production by Electrolysis. *Front. Electron.* **2021**, *2*, 11. [CrossRef]
- Bermudez, J.M.; Hannula, I. *Hydrogen—More Efforts Are Needed*; International Energy Agency (IEA): Paris, France, 2021.
- Dincer, I.; Ishaq, H. Chapter 1—Introduction. In *Renewable Hydrogen Production*; Elsevier: Amsterdam, The Netherlands, 2022; pp. 1–33, ISBN 9780323851763.
- Singh, V.; Das, D. *Potential of Hydrogen Production from Biomass*; Elsevier Inc.: Amsterdam, The Netherlands, 2018; ISBN 9780128142516.
- Kadier, A.; Kalil, M.S.; Abdesahian, P.; Chandrasekhar, K.; Mohamed, A.; Azman, N.F.; Logroño, W.; Simayi, Y.; Hamid, A.A. Recent advances and emerging challenges in microbial electrolysis cells (MECs) for microbial production of hydrogen and value-added chemicals. *Renew. Sustain. Energy Rev.* **2016**, *61*, 501–525. [CrossRef]
- Koku, H.; Eroğlu, I.; Gündüz, U.; Yücel, M.; Türker, L. Kinetics of biological hydrogen production by the photosynthetic bacterium *Rhodobacter sphaeroides* O.U. 001. *Int. J. Hydrog. Energy* **2003**, *28*, 381–388. [CrossRef]
- Eljack, F.; Kazi, M.-K. Prospects and Challenges of Green Hydrogen Economy via Multi-Sector Global Symbiosis in Qatar. *Front. Sustain.* **2021**, *1*, 612762. [CrossRef]
- Borgschulte, A. The hydrogen grand challenge. *Front. Energy Res.* **2016**, *4*, 11. [CrossRef]
- Martino, M.; Ruocco, C.; Meloni, E.; Pullumbi, P.; Palma, V. Main hydrogen production processes: An overview. *Catalysts* **2021**, *11*, 547. [CrossRef]

14. Ebrahimi, P.; Kumar, A.; Khraisheh, M. A review of recent advances in water-gas shift catalysis for hydrogen production. *Emergent Mater.* **2020**, *3*, 881–917. [[CrossRef](#)]
15. Philippot, K.; Serp, P. Concepts in Nanocatalysis. In *Nanomaterials in Catalysis*; Serp, P., Philippot, K., Eds.; WILEY-VCH: Weinheim, Germany, 2013; pp. 1–54.
16. Garcia, M.A.S.; Heyder, R.S.; Oliveira, K.C.B.; Costa, J.C.S.; Corio, P.; Gusevskaya, E.V.; dos Santos, E.N.; Bazito, R.C.; Rossi, L.M. Support Functionalization with a Phosphine-Containing Hyperbranched Polymer: A Strategy to Enhance Phosphine Grafting and Metal Loading in a Hydroformylation Catalyst. *ChemCatChem* **2016**, *8*, 1951–1960. [[CrossRef](#)]
17. Garcia, M.A.S.; Ibrahim, M.; Costa, J.C.S.; Corio, P.; Gusevskaya, E.V.; dos Santos, E.N.; Philippot, K.; Rossi, L.M. Study of the influence of PPh₃ used as capping ligand or as reaction modifier for hydroformylation reaction involving Rh NPs as precatalyst. *Appl. Catal. A Gen.* **2017**, *548*, 136–142. [[CrossRef](#)]
18. Itaciara, I.E.M.; de Sousa, S.A.A.; Laíse, L.N.; Oliveira, J.M.; Castro, K.P.R.; Costa, J.C.S.; de Moura, E.M.; de Moura, C.V.R.; Garcia, M.A.S. Au–Pd Selectivity-switchable Alcohol-oxidation Catalyst: Controlling the Duality of the Mechanism using a Multivariate Approach. *ChemCatChem* **2019**, *11*, 3022–3034. [[CrossRef](#)]
19. Franca, M.C.; Ferreira, R.M.; dos Santos Pereira, F.; e Silva, F.A.; Silva, A.C.A.; Cunha, L.C.S.; de Jesus Gomes Varela Júnior, J.; de Lima Neto, P.; Takana, A.A.; Rodrigues, T.S.; et al. Galvanic replacement managing direct methanol fuel cells: AgPt nanotubes as a strategy for methanol crossover effect tolerance. *J. Mater. Sci.* **2022**, *57*, 8225–8240. [[CrossRef](#)]
20. Cui, X.; Li, W.; Ryabchuk, P.; Junge, K.; Beller, M. Bridging homogeneous and heterogeneous catalysis by heterogeneous single-metal-site catalysts. *Nat. Catal.* **2018**, *1*, 385–397. [[CrossRef](#)]
21. Camargo, P.H.C.; Rodrigues, T.S.; da Silva, A.G.M.; Wang, J. Controlled Synthesis: Nucleation and Growth in Solution. In *Metallic Nanostructures*; Springer: Berlin/Heidelberg, Germany, 2015; pp. 49–74.
22. Costa, J.C.S.; Franco, N.; Soares, T.A.S.; Saraiva, N.A.M.; Garcia, M.A.S.; Gonzalez, J.R.; Machado, G. TiO₂ nanotubes decorated with au nanoparticles for photocatalytic hydrogen generation under UV-visible and visible light irradiations. *An. Acad. Bras. Cienc.* **2020**, *92*, 1–11. [[CrossRef](#)] [[PubMed](#)]
23. Bai, S.; Huang, B.; Shao, Q.; Huang, X. Universal Strategy for Ultrathin Pt–M (M = Fe, Co, Ni) Nanowires for Efficient Catalytic Hydrogen Generation. *ACS Appl. Mater. Interfaces* **2018**, *10*, 22257–22263. [[CrossRef](#)]
24. Shinde, D.V.; Kokumai, T.M.; Buha, J.; Prato, M.; De Trizio, L.; Manna, L. A robust and highly active hydrogen evolution catalyst based on Ru nanocrystals supported on vertically oriented Cu nanoplates. *J. Mater. Chem. A* **2020**, *8*, 10787–10795. [[CrossRef](#)]
25. Xu, P.; Lu, W.; Zhang, J.; Zhang, L. Efficient Hydrolysis of Ammonia Borane for Hydrogen Evolution Catalyzed by Plasmonic Ag@Pd Core–Shell Nanocubes. *ACS Sustain. Chem. Eng.* **2020**, *8*, 12366–12377. [[CrossRef](#)]
26. Yan, Y.; Xia, B.; Ge, X.; Liu, Z.; Wang, J.-Y.; Wang, X. Ultrathin MoS₂ Nanoplates with Rich Active Sites as Highly Efficient Catalyst for Hydrogen Evolution. *ACS Appl. Mater. Interfaces* **2013**, *5*, 12794–12798. [[CrossRef](#)] [[PubMed](#)]
27. Lee, K.; Hahn, R.; Altomare, M.; Selli, E.; Schmuki, P. Intrinsic Au Decoration of Growing TiO₂ Nanotubes and Formation of a High-Efficiency Photocatalyst for H₂ Production. *Adv. Mater.* **2013**, *25*, 6133–6137. [[CrossRef](#)] [[PubMed](#)]
28. Zhang, Y.-H.; Jiu, B.-B.; Gong, F.-L.; Chen, J.-L.; Zhang, H.-L. Morphology-controllable Cu₂O supercrystals: Facile synthesis, facet etching mechanism and comparative photocatalytic H₂ production. *J. Alloys Compd.* **2017**, *729*, 563–570. [[CrossRef](#)]
29. Li, M.; Zhang, S.; Zhao, J.; Wang, H. Maximizing Metal–Support Interactions in Pt/Co₃O₄ Nanocages to Simultaneously Boost Hydrogen Production Activity and Durability. *ACS Appl. Mater. Interfaces* **2021**, *13*, 57362–57371. [[CrossRef](#)]
30. Navakoteswara Rao, V.; Ravi, P.; Sathish, M.; Lakshmana Reddy, N.; Lee, K.; Sakar, M.; Prathap, P.; Mamatha Kumari, M.; Raghava Reddy, K.; Nadagouda, M.N.; et al. Monodispersed core/shell nanospheres of ZnS/NiO with enhanced H₂ generation and quantum efficiency at versatile photocatalytic conditions. *J. Hazard. Mater.* **2021**, *413*, 125359. [[CrossRef](#)]
31. Zhang, L.Z.; Sun, W.; Cheng, P. Spectroscopic and theoretical studies of quantum and electronic confinement effects in nanostructured materials. *Molecules* **2003**, *8*, 207–222. [[CrossRef](#)]
32. Xie, C.; Niu, Z.; Kim, D.; Li, M.; Yang, P. Surface and Interface Control in Nanoparticle Catalysis. *Chem. Rev.* **2020**, *120*, 1184–1249. [[CrossRef](#)]
33. Cao, S.; Tao, F.F.; Tang, Y.; Li, Y.; Yu, J. Size- and shape-dependent catalytic performances of oxidation and reduction reactions on nanocatalysts. *Chem. Soc. Rev.* **2016**, *45*, 4747–4765. [[CrossRef](#)]
34. Rossi, L.M.; Fiorio, J.L.; Garcia, M.A.S.; Ferraz, C.P. The role and fate of capping ligands in colloiddally prepared metal nanoparticle catalysts. *Dalt. Trans.* **2018**, *47*, 5889–5915. [[CrossRef](#)]
35. Ibrahim, M.; Garcia, M.A.S.; Vono, L.L.R.; Guerrero, M.; Lecante, P.; Rossi, L.M.; Philippot, K. Polymer: Versus phosphine stabilized Rh nanoparticles as components of supported catalysts: Implication in the hydrogenation of cyclohexene model molecule. *Dalt. Trans.* **2016**, *45*, 17782–17791. [[CrossRef](#)]
36. Carabineiro, S.A.C. Supported Gold Nanoparticles as Catalysts for the Oxidation of Alcohols and Alkanes. *Front. Chem.* **2019**, *7*, 702. [[CrossRef](#)] [[PubMed](#)]
37. Pereira, L.N.S.; Ribeiro, C.E.S.; Tofanello, A.; Costa, J.C.S.; De Moura, C.V.R.; Garcia, M.A.S.; De Moura, E.M. Gold Supported on Strontium Surface-Enriched CoFe₂O₄ Nanoparticles: A Strategy for the Selective Oxidation of Benzyl Alcohol. *J. Brazilian Chem. Soc.* **2019**, *30*, 1317–1325. [[CrossRef](#)]
38. Ilieva, L.; Petrova, P.; Pantaleo, G.; Zanella, R.; Sobczak, J.W.; Lisowski, W.; Kaszukur, Z.; Munteanu, G.; Yordanova, I.; Liotta, L.F.; et al. Alumina supported Au/Y-doped ceria catalysts for pure hydrogen production via PROX. *Int. J. Hydrogen Energy* **2019**, *44*, 233–245. [[CrossRef](#)]

39. Huang, X.; El-Sayed, M.A. Gold nanoparticles: Optical properties and implementations in cancer diagnosis and photothermal therapy. *J. Adv. Res.* **2010**, *1*, 13–28. [\[CrossRef\]](#)
40. Link, S.; El-Sayed, M.A. Size and temperature dependence of the plasmon absorption of colloidal gold nanoparticles. *J. Phys. Chem. B* **1999**, *103*, 4212–4217. [\[CrossRef\]](#)
41. Zhang, L.; Herrmann, L.O.; Baumberg, J.J. Size Dependent Plasmonic Effect on BiVO₄ Photoanodes for Solar Water Splitting. *Sci. Rep.* **2015**, *5*, 16660. [\[CrossRef\]](#)
42. Xia, Y.; Xiong, Y.; Lim, B.; Skrabalak, S.E. Shape-controlled synthesis of metal nanocrystals: Simple chemistry meets complex physics? *Angew. Chem. Int. Ed.* **2009**, *48*, 60–103. [\[CrossRef\]](#)
43. Gao, G.; Niu, X.; Xu, B.; Wang, X.L.; Yao, Y.F. Shape and size effects on photocatalytic hydrogen production: Via Pd/C₃N₄ photocatalysts under visible light. *Catal. Sci. Technol.* **2020**, *10*, 5438–5442. [\[CrossRef\]](#)
44. Vitos, L.; Ruban, A.V.; Skriver, H.L.; Kolla, J. The surface energy of metals. *Surf. Sci.* **1998**, *411*, 186–202. [\[CrossRef\]](#)
45. Geonmonond, R.S.; Da Silva, A.G.M.; Camargo, P.H.C. Controlled synthesis of noble metal nanomaterials: Motivation, principles, and opportunities in nanocatalysis. *An. Da Acad. Bras. De Ciências* **2018**, *90*, 719–744. [\[CrossRef\]](#)
46. Strasser, P.; Koh, S.; Anniyev, T.; Greeley, J.; More, K.; Yu, C.; Liu, Z.; Kaya, S.; Nordlund, D.; Ogasawara, H.; et al. Lattice-strain control of the activity in dealloyed core-shell fuel cell catalysts. *Nat. Chem.* **2010**, *2*, 454–460. [\[CrossRef\]](#) [\[PubMed\]](#)
47. Li, G.; Zhang, W.; Luo, N.; Xue, Z.; Hu, Q.; Zeng, W.; Xu, J. Bimetallic nanocrystals: Structure, controllable synthesis and applications in catalysis, energy and sensing. *Nanomaterials* **2021**, *11*, 1926. [\[CrossRef\]](#) [\[PubMed\]](#)
48. Gilroy, K.D.; Ruditskiy, A.; Peng, H.C.; Qin, D.; Xia, Y. Bimetallic nanocrystals: Syntheses, properties, and applications. *Chem. Rev.* **2016**, *116*, 10414–10472. [\[CrossRef\]](#) [\[PubMed\]](#)
49. Kim, H.Y.; Muthurasu, A.; Chhetri, K.; Dahal, B. Ruthenium Nanoparticles-Integrated Bimetallic Metal-Organic Frameworks Electrocatalysts for Multifunctional Electrode Materials and Practical Water Electrolysis in Seawater. *Nanoscale* **2022**, *14*, 6557–6569. [\[CrossRef\]](#)
50. Li, L.; Zhang, G.; Wang, B.; Yang, T.; Yang, S. Electrochemical formation of PtRu bimetallic nanoparticles for highly efficient and pH-universal hydrogen evolution reaction. *J. Mater. Chem. A* **2020**, *8*, 2090–2098. [\[CrossRef\]](#)
51. Lu, X.F.; Zhang, S.L.; Sim, W.L.; Gao, S.; Lou, X.W. Phosphorized CoNi₂S₄ Yolk-Shell Spheres for Highly Efficient Hydrogen Production via Water and Urea Electrolysis. *Angew. Chem. Int. Ed.* **2021**, *60*, 22885–22891. [\[CrossRef\]](#)
52. Cortés, E.; Besteiro, L.V.; Alabastri, A.; Baldi, A.; Tagliabue, G.; Demetriadou, A.; Narang, P. Challenges in Plasmonic Catalysis. *ACS Nano* **2020**, *14*, 16202–16219. [\[CrossRef\]](#)
53. Araujo, T.P.; Quiroz, J.; Barbosa, E.C.M.; Camargo, P.H.C. Understanding plasmonic catalysis with controlled nanomaterials based on catalytic and plasmonic metals. *Curr. Opin. Colloid Interface Sci.* **2019**, *39*, 110–122. [\[CrossRef\]](#)
54. Ezendam, S.; Herran, M.; Nan, L.; Gruber, C.; Kang, Y.; Gröbmeyer, F.; Lin, R.; Gargiulo, J.; Sousa-Castillo, A.; Cortés, E. Hybrid Plasmonic Nanomaterials for Hydrogen Generation and Carbon Dioxide Reduction. *ACS Energy Lett.* **2022**, *7*, 778–815. [\[CrossRef\]](#)
55. da Silva, A.G.M.; Rodrigues, T.S.; Wang, J.; Camargo, P.H.C. Plasmonic catalysis with designer nanoparticles. *Chem. Commun.* **2022**, *58*, 2055–2074. [\[CrossRef\]](#)
56. Christopher, P.; Xin, H.; Marimuthu, A.; Linic, S. Singular characteristics and unique chemical bond activation mechanisms of photocatalytic reactions on plasmonic nanostructures. *Nat. Mater.* **2012**, *11*, 1044–1050. [\[CrossRef\]](#) [\[PubMed\]](#)
57. Mo, J.; Barbosa, E.C.M.; Wu, S.; Li, Y.; Sun, Y.; Xiang, W.; Li, T.; Pu, S.; Robertson, A.; Wu, T.-S.; et al. Atomic-Precision Tailoring of Au–Ag Core–Shell Composite Nanoparticles for Direct Electrochemical-Plasmonic Hydrogen Evolution in Water Splitting. *Adv. Funct. Mater.* **2021**, *31*, 2102517. [\[CrossRef\]](#)
58. Osman, A.I.; Mehta, N.; Elgarahy, A.M.; Hefny, M.; Al-Hinai, A.; Al-Muhtaseb, A.H.; Rooney, D.W. *Hydrogen Production, Storage, Utilisation and Environmental Impacts: A Review*; Springer International Publishing: Berlin/Heidelberg, Germany, 2021; ISBN 0123456789.
59. El-Shafie, M.; Kambara, S.; Hayakawa, Y. Hydrogen Production Technologies Overview. *J. Power Energy Eng.* **2019**, *7*, 107–154. [\[CrossRef\]](#)
60. Basile, A.; Liguori, S.; Iulianelli, A. *Membrane Reactors for Methane Steam Reforming (MSR)*; Elsevier Ltd.: Amsterdam, The Netherlands, 2015; ISBN 9781782422273.
61. Mortensen, P.M.; Dybkjær, I. Industrial scale experience on steam reforming of CO₂-rich gas. *Appl. Catal. A Gen.* **2015**, *495*, 141–151. [\[CrossRef\]](#)
62. Han, B.; Wang, F.; Zhang, L.; Wang, Y.; Fan, W.; Xu, L.; Yu, H.; Li, Z. Syngas production from methane steam reforming and dry reforming reactions over sintering-resistant Ni@SiO₂ catalyst. *Res. Chem. Intermed.* **2020**, *46*, 1735–1748. [\[CrossRef\]](#)
63. Sasson Bitters, J.; He, T.; Nestler, E.; Senanayake, S.D.; Chen, J.G.; Zhang, C. Utilizing bimetallic catalysts to mitigate coke formation in dry reforming of methane. *J. Energy Chem.* **2022**, *68*, 124–142. [\[CrossRef\]](#)
64. Nambo, A.; Atla, V.; Vasireddy, S.; Kumar, V.; Jasinski, J.B.; Upadhyayula, S.; Sunkara, M. Nanowire-based materials as coke-resistant catalyst supports for dry methane reforming. *Catalysts* **2021**, *11*, 175. [\[CrossRef\]](#)
65. Meloni, E.; Martino, M.; Palma, V. A Short Review on Ni Based Catalysts and Related Engineering Issues for Methane Steam Reforming. *Catalysts* **2020**, *10*, 352. [\[CrossRef\]](#)
66. Vinum, M.G.; Almind, M.R.; Engbæk, J.S.; Vendelbo, S.B.; Hansen, M.F.; Frandsen, C.; Bendix, J.; Mortensen, P.M. Dual-Function Cobalt–Nickel Nanoparticles Tailored for High-Temperature Induction-Heated Steam Methane Reforming. *Angew. Chemie Int. Ed.* **2018**, *57*, 10569–10573. [\[CrossRef\]](#)

67. Jang, W.J.; Shim, J.O.; Kim, H.M.; Yoo, S.Y.; Roh, H.S. A review on dry reforming of methane in aspect of catalytic properties. *Catal. Today* **2019**, *324*, 15–26. [\[CrossRef\]](#)
68. Aramouni, N.A.K.; Touma, J.G.; Tarboush, B.A.; Zeaiter, J.; Ahmad, M.N. Catalyst design for dry reforming of methane: Analysis review. *Renew. Sustain. Energy Rev.* **2018**, *82*, 2570–2585. [\[CrossRef\]](#)
69. Usman, M.; Wan Daud, W.M.A.; Abbas, H.F. Dry reforming of methane: Influence of process parameters—A review. *Renew. Sustain. Energy Rev.* **2015**, *45*, 710–744. [\[CrossRef\]](#)
70. Gucci, L.; Stefler, G.; Geszti, O.; Sajó, I.; Pászti, Z.; Tompos, A.; Schay, Z. Methane dry reforming with CO₂: A study on surface carbon species. *Appl. Catal. A Gen.* **2010**, *375*, 236–246. [\[CrossRef\]](#)
71. Zeng, S.; Zhang, L.; Zhang, X.; Wang, Y.; Pan, H.; Su, H. Modification effect of natural mixed rare earths on Co/ γ -Al₂O₃ catalysts for CH₄/CO₂ reforming to synthesis gas. *Int. J. Hydrog. Energy* **2012**, *37*, 9994–10001. [\[CrossRef\]](#)
72. Zhou, L.; Martinez, J.M.P.; Finzel, J.; Zhang, C.; Swearer, D.F.; Tian, S.; Robatjazi, H.; Lou, M.; Dong, L.; Henderson, L.; et al. Light-driven methane dry reforming with single atomic site antenna-reactor plasmonic photocatalysts. *Nat. Energy* **2020**, *5*, 61–70. [\[CrossRef\]](#)
73. Niu, J.; Wang, Y.; Qi, Y.; Dam, A.H.; Wang, H.; Zhu, Y.A.; Holmen, A.; Ran, J.; Chen, D. New mechanism insights into methane steam reforming on Pt/Ni from DFT and experimental kinetic study. *Fuel* **2020**, *266*, 117143. [\[CrossRef\]](#)
74. Azancot, L.; Bobadilla, L.F.; Santos, J.L.; Córdoba, J.M.; Centeno, M.A.; Odriozola, J.A. Influence of the preparation method in the metal-support interaction and reducibility of Ni-Mg-Al based catalysts for methane steam reforming. *Int. J. Hydrog. Energy* **2019**, *44*, 19827–19840. [\[CrossRef\]](#)
75. Montini, T.; Melchionna, M.; Monai, M.; Fornasiero, P. Fundamentals and Catalytic Applications of CeO₂-Based Materials. *Chem. Rev.* **2016**, *116*, 5987–6041. [\[CrossRef\]](#)
76. Safavina, B.; Wang, Y.; Jiang, C.; Roman, C.; Darapaneni, P.; Larriviere, J.; Cullen, D.A.; Dooley, K.M.; Dorman, J.A. Enhancing Ce_xZr_{1-x}O₂ Activity for Methane Dry Reforming Using Subsurface Ni Dopants. *ACS Catal.* **2020**, *10*, 4070–4079. [\[CrossRef\]](#)
77. Damaskinos, C.M.; Vasiliades, M.A.; Stathopoulos, V.N.; Efstathiou, A.M. The Effect of CeO₂ Preparation Method on the Carbon Pathways in the Dry Reforming of Methane on Ni/CeO₂ Studied by Transient Techniques. *Catalysts* **2019**, *9*, 621. [\[CrossRef\]](#)
78. Ni, Z.; Djitchou, X.; Gao, X.; Wang, J.; Liu, H.; Zhang, Q. Effect of preparation methods of CeO₂ on the properties and performance of Ni/CeO₂ in CO₂ reforming of CH₄. *Sci. Rep.* **2022**, *12*, 5344. [\[CrossRef\]](#)
79. Wang, N.; Qian, W.; Chu, W.; Wei, F. Crystal-plane effect of nanoscale CeO₂ on the catalytic performance of Ni/CeO₂ catalysts for methane dry reforming. *Catal. Sci. Technol.* **2016**, *6*, 3594–3605. [\[CrossRef\]](#)
80. Tu, P.H.; Le, D.N.; Dao, T.D.; Tran, Q.T.; Doan, T.C.D.; Shiratori, Y.; Dang, C.M. Paper-structured catalyst containing CeO₂-Ni flowers for dry reforming of methane. *Int. J. Hydrog. Energy* **2020**, *45*, 18363–18375. [\[CrossRef\]](#)
81. He, L.; Ren, Y.; Fu, Y.; Yue, B.; Edman Tsang, S.C.; He, H. Morphology-dependent catalytic activity of Ru/CeO₂ in dry reforming of methane. *Molecules* **2019**, *24*, 526. [\[CrossRef\]](#)
82. Anil, S.; Indrāja, S.; Singh, R.; Appari, S.; Roy, B. A review on ethanol steam reforming for hydrogen production over Ni/Al₂O₃ and Ni/CeO₂ based catalyst powders. *Int. J. Hydrog. Energy* **2022**, *47*, 8177–8213. [\[CrossRef\]](#)
83. Shtyka, O.; Dimitrova, Z.; Ciesielski, R.; Kedziora, A.; Mitukiewicz, G.; Leyko, J.; Maniukiewicz, W.; Czyłkowska, A.; Maniecki, T. Steam reforming of ethanol for hydrogen production: Influence of catalyst composition (Ni/Al₂O₃, Ni/Al₂O₃-CeO₂, Ni/Al₂O₃-ZnO) and process conditions. *React. Kinet. Mech. Catal.* **2021**, *132*, 907–919. [\[CrossRef\]](#)
84. Liu, X.; Zhou, K.; Wang, L.; Wang, B.; Li, Y. Oxygen vacancy clusters promoting reducibility and activity of ceria nanorods. *J. Am. Chem. Soc.* **2009**, *131*, 3140–3141. [\[CrossRef\]](#)
85. Xiao, Z.; Li, Y.; Hou, F.; Wu, C.; Pan, L.; Zou, J.; Wang, L.; Zhang, X.; Liu, G.; Li, G. Engineering oxygen vacancies and nickel dispersion on CeO₂ by Pr doping for highly stable ethanol steam reforming. *Appl. Catal. B Environ.* **2019**, *258*, 117940. [\[CrossRef\]](#)
86. Xiao, Z.; Wu, C.; Wang, L.; Xu, J.; Zheng, Q.; Pan, L.; Zou, J.; Zhang, X.; Li, G. Boosting hydrogen production from steam reforming of ethanol on nickel by lanthanum doped ceria. *Appl. Catal. B Environ.* **2021**, *286*, 119884. [\[CrossRef\]](#)
87. Sun, C.; Li, H.; Chen, L. Nanostructured ceria-based materials: Synthesis, properties, and applications. *Energy Environ. Sci.* **2012**, *5*, 8475–8505. [\[CrossRef\]](#)
88. Sohn, H.; Ozkan, U.S. Cobalt-Based Catalysts for Ethanol Steam Reforming: An Overview. *Energy Fuels* **2016**, *30*, 5309–5322. [\[CrossRef\]](#)
89. Wang, Y.; Zhu, S.; He, S.; Lu, J.; Liu, J.; Lu, H.; Song, D.; Luo, Y. Nanoarchitectonics of Ni/CeO₂ Catalysts: The Effect of Pretreatment on the Low-Temperature Steam Reforming of Glycerol. *Nanomaterials* **2022**, *12*, 816. [\[CrossRef\]](#)
90. Zanchet, D.; Santos, J.B.O.; Damyanova, S.; Gallo, J.M.R.; Bueno, J.M.C. Toward understanding metal-catalyzed ethanol reforming. *ACS Catal.* **2015**, *5*, 3841–3863. [\[CrossRef\]](#)
91. Borges, L.R.; da Silva, A.G.M.; Braga, A.H.; Rossi, L.M.; Suller Garcia, M.A.; Vidinha, P. Towards the Effect of Pt⁰/Pt^{δ+} and Ce³⁺ Species at the Surface of CeO₂ Crystals: Understanding the Nature of the Interactions under CO Oxidation Conditions. *ChemCatChem* **2021**, *13*, 1340–1354. [\[CrossRef\]](#)
92. Araiza, D.G.; Gómez-Cortés, A.; Díaz, G. Effect of ceria morphology on the carbon deposition during steam reforming of ethanol over Ni/CeO₂ catalysts. *Catal. Today* **2020**, *349*, 235–243. [\[CrossRef\]](#)
93. Moraes, T.S.; Neto, R.C.R.; Ribeiro, M.C.; Mattos, L.V.; Kourtelesis, M.; Verykios, X.; Noronha, F.B. Effects of ceria morphology on catalytic performance of Ni/CeO₂ catalysts for low temperature steam reforming of ethanol. *Top. Catal.* **2015**, *58*, 281–294. [\[CrossRef\]](#)

94. Yang, S.; Zhou, F.; Liu, Y.; Zhang, L.; Chen, Y.; Wang, H.; Tian, Y.; Zhang, C.; Liu, D. Morphology effect of ceria on the performance of CuO/CeO₂ catalysts for hydrogen production by methanol steam reforming. *Int. J. Hydrog. Energy* **2019**, *44*, 7252–7261. [\[CrossRef\]](#)
95. Silva, A.G.M.; Rodrigues, T.S.; Dias, A.; Fajardo, H.V.; Goncalves, R.F.; Godinho, M.; Robles-Dutenhefner, P.A. Ce_{1-x}Sm_xO_{1.9-δ} nanoparticles obtained by microwave-assisted hydrothermal processing: An efficient application for catalytic oxidation of [small alpha]-bisabolol. *Catal. Sci. Technol.* **2014**, *4*, 814–821. [\[CrossRef\]](#)
96. Da Silva, A.G.M.; Batalha, D.C.; Rodrigues, T.S.; Candido, E.G.; Luz, S.C.; De Freitas, I.C.; Fonseca, F.C.; De Oliveira, D.C.; Taylor, J.G.; De Torresi, S.I.C.; et al. Sub-15 nm CeO₂ nanowires as an efficient non-noble metal catalyst in the room-temperature oxidation of aniline. *Catal. Sci. Technol.* **2018**, *8*, 1828–1839. [\[CrossRef\]](#)
97. Rodrigues, T.S.; de Moura, A.B.L.; e Silva, F.A.; Candido, E.G.; da Silva, A.G.M.; de Oliveira, D.C.; Quiroz, J.; Camargo, P.H.C.; Bergamaschi, V.S.; Ferreira, J.C.; et al. Ni supported Ce_{0.9}Sm_{0.1}O_{2-Δ} nanowires: An efficient catalyst for ethanol steam reforming for hydrogen production. *Fuel* **2019**, *237*, 1244–1253. [\[CrossRef\]](#)
98. Wang, F.; Zhang, L.; Zhu, J.; Han, B.; Zhao, L.; Yu, H.; Deng, Z.; Shi, W. Study on different CeO₂ structure stability during ethanol steam reforming reaction over Ir/CeO₂ nanocatalysts. *Appl. Catal. A Gen.* **2018**, *564*, 226–233. [\[CrossRef\]](#)
99. Kourtelesis, M.; Moraes, T.S.; Mattos, L.V.; Niakolas, D.K.; Noronha, F.B.; Verykios, X. The effects of support morphology on the performance of Pt/CeO₂ catalysts for the low temperature steam reforming of ethanol. *Appl. Catal. B Environ.* **2021**, *284*, 119757. [\[CrossRef\]](#)
100. Ratnasamy, C.; Wagner, J.P. Water Gas Shift Catalysis. *Catal. Rev.* **2009**, *51*, 325–440. [\[CrossRef\]](#)
101. Liang, J.; Lin, J.; Liu, J.; Wang, X.; Zhang, T.; Li, J. Dual Metal Active Sites in an Ir₁/FeO_x Single-Atom Catalyst: A Redox Mechanism for the Water-Gas Shift Reaction. *Angew. Chem. Int. Ed.* **2020**, *59*, 12868–12875. [\[CrossRef\]](#) [\[PubMed\]](#)
102. Chen, W.-H.; Chen, C.-Y. Water gas shift reaction for hydrogen production and carbon dioxide capture: A review. *Appl. Energy* **2020**, *258*, 114078. [\[CrossRef\]](#)
103. Rodriguez, J.A.; Ramirez, P.J.; Asara, G.G.; Viñes, F.; Evans, J.; Liu, P.; Ricart, J.M.; Illas, F. Charge Polarization at a Au-TiC Interface and the Generation of Highly Active and Selective Catalysts for the Low-Temperature Water-Gas Shift Reaction. *Angew. Chem. Int. Ed.* **2014**, *53*, 11270–11274. [\[CrossRef\]](#)
104. Chen, W.-H.; Jheng, J.-G.; Yu, A.B. Hydrogen generation from a catalytic water gas shift reaction under microwave irradiation. *Int. J. Hydrog. Energy* **2008**, *33*, 4789–4797. [\[CrossRef\]](#)
105. Chen, W.-H.; Syu, Y.-J. Hydrogen production from water gas shift reaction in a high gravity (Higee) environment using a rotating packed bed. *Int. J. Hydrog. Energy* **2010**, *35*, 10179–10189. [\[CrossRef\]](#)
106. Sastre, F.; Oteri, M.; Corma, A.; García, H. Photocatalytic water gas shift using visible or simulated solar light for the efficient, room-temperature hydrogen generation. *Energy Environ. Sci.* **2013**, *6*, 2211. [\[CrossRef\]](#)
107. Zhao, L.; Qi, Y.; Song, L.; Ning, S.; Ouyang, S.; Xu, H.; Ye, J. Solar-Driven Water–Gas Shift Reaction over CuO_x/Al₂O₃ with 1.1 % of Light-to-Energy Storage. *Angew. Chem.* **2019**, *131*, 7790–7794. [\[CrossRef\]](#)
108. de Lucas-Consuegra, A.; Caravaca, A.; González-Cobos, J.; Valverde, J.L.; Dorado, F. Electrochemical activation of a non noble metal catalyst for the water–gas shift reaction. *Catal. Commun.* **2011**, *15*, 6–9. [\[CrossRef\]](#)
109. Cui, X.; Su, H.-Y.; Chen, R.; Yu, L.; Dong, J.; Ma, C.; Wang, S.; Li, J.; Yang, F.; Xiao, J.; et al. Room-temperature electrochemical water–gas shift reaction for high purity hydrogen production. *Nat. Commun.* **2019**, *10*, 86. [\[CrossRef\]](#) [\[PubMed\]](#)
110. Chen, W.-H.; Chiu, T.-W.; Hung, C.-I. Hydrogen production from methane under the interaction of catalytic partial oxidation, water gas shift reaction and heat recovery. *Int. J. Hydrog. Energy* **2010**, *35*, 12808–12820. [\[CrossRef\]](#)
111. Chou, C.Y.; Loiland, J.A.; Lobo, R.F. Reverse Water-Gas Shift Iron Catalyst Derived from Magnetite. *Catalysts* **2019**, *9*, 773. [\[CrossRef\]](#)
112. Zhu, M.; Wachs, I.E. Iron-Based Catalysts for the High-Temperature Water–Gas Shift (HT-WGS) Reaction: A Review. *ACS Catal.* **2016**, *6*, 722–732. [\[CrossRef\]](#)
113. Ren, Z.; Peng, F.; Li, J.; Liang, X.; Chen, B. Morphology-dependent properties of Cu/CEO₂ catalysts for the water-gas shift reaction. *Catalysts* **2017**, *7*, 48. [\[CrossRef\]](#)
114. Yan, H.; Qin, X.-T.; Yin, Y.; Teng, Y.-F.; Jin, Z.; Jia, C.-J. Promoted Cu-Fe₃O₄ catalysts for low-temperature water gas shift reaction: Optimization of Cu content. *Appl. Catal. B Environ.* **2018**, *226*, 182–193. [\[CrossRef\]](#)
115. Jha, A.; Jeong, D.-W.; Shim, J.-O.; Jang, W.-J.; Lee, Y.-L.; Rode, C.V.; Roh, H.-S. Hydrogen production by the water-gas shift reaction using CuNi/Fe₂O₃ catalyst. *Catal. Sci. Technol.* **2015**, *5*, 2752–2760. [\[CrossRef\]](#)
116. Ang, M.L.; Oemar, U.; Kathiraser, Y.; Saw, E.T.; Lew, C.H.K.; Du, Y.; Borgna, A.; Kawi, S. High-temperature water–gas shift reaction over Ni/xK/CeO₂ catalysts: Suppression of methanation via formation of bridging carbonyls. *J. Catal.* **2015**, *329*, 130–143. [\[CrossRef\]](#)
117. Zhu, S.; Wang, H.; Wan, K.; Guo, L.-J.; He, T.; Shi, X. Water–Gas Shift Reaction on Titania-Supported Single-Metal-Atom Catalysts: The Role of Cation (Ti) and Oxygen Vacancy. *J. Phys. Chem. C* **2021**, *125*, 8620–8629. [\[CrossRef\]](#)
118. Thouchprasitchai, N.; Luengnaruemitchai, A.; Pongstabodee, S. Water-gas shift reaction over Cu–Zn, Cu–Fe, and Cu–Zn–Fe composite-oxide catalysts prepared by urea-nitrate combustion. *J. Ind. Eng. Chem.* **2013**, *19*, 1483–1492. [\[CrossRef\]](#)
119. Hu, J.; Guo, W.; Liu, Z.-H.; Lu, X.; Zhu, H.; Shi, F.; Yan, J.; Jiang, R. Unraveling the Mechanism of the Zn-Improved Catalytic Activity of Pd-Based Catalysts for Water–Gas Shift Reaction. *J. Phys. Chem. C* **2016**, *120*, 20181–20191. [\[CrossRef\]](#)

120. Na, H.-S.; Ahn, C.-I.; Jha, A.; Park, K.S.; Jang, W.-J.; Shim, J.-O.; Jeong, D.-W.; Roh, H.-S.; Bae, J.W. The investigation of non-noble metal doped mesoporous cobalt oxide catalysts for the water-gas shift reaction. *RSC Adv.* **2016**, *6*, 52754–52760. [\[CrossRef\]](#)
121. Majima, T.; Kono, E.; Ogo, S.; Sekine, Y. Pre-reduction and K loading effects on noble metal free Co-system catalyst for water gas shift reaction. *Appl. Catal. A Gen.* **2016**, *523*, 92–96. [\[CrossRef\]](#)
122. Luo, W.; Chen, Y.; Du, Z.; Chen, C. Theoretical Study on PdCu/CeO₂-Catalyzed Water–Gas Shift Reaction: Crucial Role of the Metal/Ceria Interface and O₂ Enhancement Effects. *J. Phys. Chem. C* **2018**, *122*, 28868–28883. [\[CrossRef\]](#)
123. Zhang, Z.; Wang, S.-S.; Song, R.; Cao, T.; Luo, L.; Chen, X.; Gao, Y.; Lu, J.; Li, W.-X.; Huang, W. The most active Cu facet for low-temperature water gas shift reaction. *Nat. Commun.* **2017**, *8*, 488. [\[CrossRef\]](#)
124. Li, Z.; Li, N.; Wang, N.; Zhou, B.; Yin, P.; Song, B.; Yu, J.; Yang, Y. Mechanism Investigations on Water Gas Shift Reaction over Cu(111), Cu(100), and Cu(211) Surfaces. *ACS Omega* **2022**, *7*, 3514–3521. [\[CrossRef\]](#)
125. Lykaki, M.; Stefa, S.; Carabineiro, S.A.C.; Soria, M.A.; Madeira, L.M.; Konsolakis, M. Shape effects of ceria nanoparticles on the water-gas shift performance of CuOx/CeO₂ catalysts. *Catalysts* **2021**, *11*, 753. [\[CrossRef\]](#)
126. Knudsen, J.; Nilekar, A.U.; Vang, R.T.; Schnadt, J.; Kunkes, E.L.; Dumesic, J.A.; Mavrikakis, M.; Besenbacher, F. A Cu/Pt Near-Surface Alloy for Water–Gas Shift Catalysis. *J. Am. Chem. Soc.* **2007**, *129*, 6485–6490. [\[CrossRef\]](#)
127. Fu, X.-P.; Guo, L.-W.; Wang, W.-W.; Ma, C.; Jia, C.-J.; Wu, K.; Si, R.; Sun, L.-D.; Yan, C.-H. Direct Identification of Active Surface Species for the Water–Gas Shift Reaction on a Gold–Ceria Catalyst. *J. Am. Chem. Soc.* **2019**, *141*, 4613–4623. [\[CrossRef\]](#)
128. Chen, Y.; Lin, J.; Li, L.; Qiao, B.; Liu, J.; Su, Y.; Wang, X. Identifying Size Effects of Pt as Single Atoms and Nanoparticles Supported on FeO_x for the Water-Gas Shift Reaction. *ACS Catal.* **2018**, *8*, 859–868. [\[CrossRef\]](#)
129. Rivero-Crespo, M.A.; Mon, M.; Ferrando-Soria, J.; Lopes, C.W.; Boronat, M.; Leyva-Pérez, A.; Corma, A.; Hernández-Garrido, J.C.; López-Haro, M.; Calvino, J.J.; et al. Confined Pt 1+ Water Clusters in a MOF Catalyze the Low-Temperature Water–Gas Shift Reaction with both CO₂ Oxygen Atoms Coming from Water. *Angew. Chem. Int. Ed.* **2018**, *57*, 17094–17099. [\[CrossRef\]](#) [\[PubMed\]](#)
130. Ding, K.; Gulec, A.; Johnson, A.M.; Schweitzer, N.M.; Stucky, G.D.; Marks, L.D.; Stair, P.C. Identification of active sites in CO oxidation and water-gas shift over supported Pt catalysts. *Science* **2015**, *350*, 189–192. [\[CrossRef\]](#) [\[PubMed\]](#)
131. Ammal, S.C.; Heyden, A. Understanding the Nature and Activity of Supported Platinum Catalysts for the Water–Gas Shift Reaction: From Metallic Nanoclusters to Alkali-Stabilized Single-Atom Cations. *ACS Catal.* **2019**, *9*, 7721–7740. [\[CrossRef\]](#)
132. Chen, J.-J.; Li, X.-N.; Liu, Q.-Y.; Wei, G.-P.; Yang, Y.; Li, Z.-Y.; He, S.-G. Water Gas Shift Reaction Catalyzed by Rhodium–Manganese Oxide Cluster Anions. *J. Phys. Chem. Lett.* **2021**, *12*, 8513–8520. [\[CrossRef\]](#)
133. Lei, Y.; Cant, N.; Trimm, D. The origin of rhodium promotion of Fe₃O₄–Cr₂O₃ catalysts for the high-temperature water–gas shift reaction. *J. Catal.* **2006**, *239*, 227–236. [\[CrossRef\]](#)
134. Shekhar, M.; Wang, J.; Lee, W.-S.; Williams, W.D.; Kim, S.M.; Stach, E.A.; Miller, J.T.; Delgass, W.N.; Ribeiro, F.H. Size and Support Effects for the Water–Gas Shift Catalysis over Gold Nanoparticles Supported on Model Al₂O₃ and TiO₂. *J. Am. Chem. Soc.* **2012**, *134*, 4700–4708. [\[CrossRef\]](#)
135. Fu, Q.; Saltsburg, H.; Flytzani-Stephanopoulos, M. Active nonmetallic Au and Pt species on ceria-based water-gas shift catalysts. *Science* **2003**, *301*, 935–938. [\[CrossRef\]](#)
136. Yao, S.; Zhang, X.; Zhou, W.; Gao, R.; Xu, W.; Ye, Y.; Lin, L.; Wen, X.; Liu, P.; Chen, B.; et al. Atomic-layered Au clusters on α-MoC as catalysts for the low-temperature water-gas shift reaction. *Science* **2017**, *357*, 389–393. [\[CrossRef\]](#)
137. Tao, F.; Ma, Z. Water–gas shift on gold catalysts: Catalyst systems and fundamental studies. *Phys. Chem. Chem. Phys.* **2013**, *15*, 15260. [\[CrossRef\]](#)
138. Arab, A.; Sharafie, D.; Fazli, M. Theoretical study of water-gas shift reaction on the silver nanocluster. *J. Phys. Chem. Solids* **2017**, *109*, 100–108. [\[CrossRef\]](#)
139. Zugic, B.; Zhang, S.; Bell, D.C.; Tao, F.; Flytzani-Stephanopoulos, M. Probing the Low-Temperature Water–Gas Shift Activity of Alkali-Promoted Platinum Catalysts Stabilized on Carbon Supports. *J. Am. Chem. Soc.* **2014**, *136*, 3238–3245. [\[CrossRef\]](#) [\[PubMed\]](#)
140. Bi, Y.; Xu, H.; Li, W.; Goldbach, A. Water–gas shift reaction in a Pd membrane reactor over Pt/Ce_{0.6}Zr_{0.4}O₂ catalyst. *Int. J. Hydrog. Energy* **2009**, *34*, 2965–2971. [\[CrossRef\]](#)
141. Huang, S.-C.; Lin, C.-H.; Wang, J.-H. Trends of Water Gas Shift Reaction on Close-Packed Transition Metal Surfaces. *J. Phys. Chem. C* **2010**, *114*, 9826–9834. [\[CrossRef\]](#)
142. Schweitzer, N.M.; Schaidle, J.A.; Ezekoye, O.K.; Pan, X.; Linic, S.; Thompson, L.T. High Activity Carbide Supported Catalysts for Water Gas Shift. *J. Am. Chem. Soc.* **2011**, *133*, 2378–2381. [\[CrossRef\]](#)
143. Si, R.; Flytzani-Stephanopoulos, M. Shape and Crystal-Plane Effects of Nanoscale Ceria on the Activity of Au–CeO₂ Catalysts for the Water–Gas Shift Reaction. *Angew. Chem. Int. Ed.* **2008**, *47*, 2884–2887. [\[CrossRef\]](#)
144. Guan, Y.; Lighthart, D.A.J.M.; Pirgon-Galin, Ö.; Pieterse, J.A.Z.; van Santen, R.A.; Hensen, E.J.M. Gold Stabilized by Nanostructured Ceria Supports: Nature of the Active Sites and Catalytic Performance. *Top. Catal.* **2011**, *54*, 424–438. [\[CrossRef\]](#)
145. Lee, Y.L.; Mnoyan, A.; Na, H.S.; Ahn, S.Y.; Kim, K.J.; Shim, J.O.; Lee, K.; Roh, H.S. Comparison of the effects of the catalyst preparation method and CeO₂ morphology on the catalytic activity of Pt/CeO₂ catalysts for the water-gas shift reaction. *Catal. Sci. Technol.* **2020**, *10*, 6299–6308. [\[CrossRef\]](#)
146. Li, Y.; Kottwitz, M.; Vincent, J.L.; Enright, M.J.; Liu, Z.; Zhang, L.; Huang, J.; Senanayake, S.D.; Yang, W.C.D.; Crozier, P.A.; et al. Dynamic structure of active sites in ceria-supported Pt catalysts for the water gas shift reaction. *Nat. Commun.* **2021**, *12*, 914. [\[CrossRef\]](#)

147. Baschuk, J.J.; Li, X. Carbon monoxide poisoning of proton exchange membrane fuel cells. *Int. J. Energy Res.* **2001**, *25*, 695–713. [CrossRef]
148. Teixeira, M.; Madeira, L.M.; Sousa, J.M.; Mendes, A. Modeling of a catalytic membrane reactor for CO removal from hydrogen streams—A theoretical study. *Int. J. Hydrog. Energy* **2010**, *35*, 11505–11513. [CrossRef]
149. Dagle, R.A.; Karim, A.; Li, G.; Su, Y.; King, D.L. *Syngas Conditioning*; Elsevier B.V.: Amsterdam, The Netherlands, 2011; ISBN 9780444535634. [CrossRef]
150. Tabakova, T. Recent Advances in Design of Gold-Based Catalysts for H₂ Clean-Up Reactions. *Front. Chem.* **2019**, *7*, 517. [CrossRef] [PubMed]
151. Al Soubaihi, R.M.; Saoud, K.M.; Dutta, J. Critical review of low-temperature CO oxidation and hysteresis phenomenon on heterogeneous catalysts. *Catalysts* **2018**, *8*, 660. [CrossRef]
152. Hernández, J.A.; Gómez, S.A.; Zepeda, T.A.; Fierro-González, J.C.; Fuentes, G.A. Insight into the Deactivation of Au/CeO₂ Catalysts Studied by in Situ Spectroscopy during the CO-PROX Reaction. *ACS Catal.* **2015**, *5*, 4003–4012. [CrossRef]
153. Liu, Y.; Fu, Q.; Stephanopoulos, M.F. Preferential oxidation of CO in H₂ over CuO-CeO₂ catalysts. *Catal. Today* **2004**, *93*, 241–246. [CrossRef]
154. Santos, D.M.F.; Sequeira, C.A.C.; Figueiredo, J.L. Hydrogen production by alkaline water electrolysis. *Quim. Nova* **2013**, *36*, 1176–1193. [CrossRef]
155. Pagliaro, M.; Konstandopoulos, A.G.; Ciriminna, R.; Palmisano, G. Solar hydrogen: Fuel of the near future. *Energy Environ. Sci.* **2010**, *3*, 279–287. [CrossRef]
156. Mahmood, N.; Yao, Y.; Zhang, J.W.; Pan, L.; Zhang, X.; Zou, J.J. Electrocatalysts for Hydrogen Evolution in Alkaline Electrolytes: Mechanisms, Challenges, and Prospective Solutions. *Adv. Sci.* **2018**, *5*, 1700464. [CrossRef]
157. Zheng, Y.; Jiao, Y.; Vasileff, A.; Qiao, S.Z. The Hydrogen Evolution Reaction in Alkaline Solution: From Theory, Single Crystal Models, to Practical Electrocatalysts. *Angew. Chem. Int. Ed.* **2018**, *57*, 7568–7579. [CrossRef]
158. Đurovič, M.; Hnát, J.; Bouzek, K. Electrocatalysts for the hydrogen evolution reaction in alkaline and neutral media. A comparative review. *J. Power Sources* **2021**, *493*, 229708. [CrossRef]
159. Santos, A.L.; Cebola, M.J.; Santos, D.M.F. Towards the hydrogen economy—A review of the parameters that influence the efficiency of alkaline water electrolyzers. *Energies* **2021**, *14*, 3193. [CrossRef]
160. Dezem, V. Why Hydrogen Is the Hottest Thing in Green Energy 2021. Available online: <https://illuminem.com/post/96ed8c14-6f8b-4c90-8602-d36f92d5af1b> (accessed on 28 April 2022).
161. Wang, S.; Lu, A.; Zhong, C.J. Hydrogen production from water electrolysis: Role of catalysts. *Nano Conver.* **2021**, *8*, 4. [CrossRef] [PubMed]
162. Hao, Y.M.; Nakajima, H.; Inada, A.; Sasaki, K.; Ito, K. Overpotentials and reaction mechanism in electrochemical hydrogen pumps. *Electrochim. Acta* **2019**, *301*, 274–283. [CrossRef]
163. Zhu, J.; Hu, L.; Zhao, P.; Lee, L.Y.S.; Wong, K.Y. Recent Advances in Electrocatalytic Hydrogen Evolution Using Nanoparticles. *Chem. Rev.* **2020**, *120*, 851–918. [CrossRef] [PubMed]
164. Roger, B.Y. The rate of electrolytic hydrogen and the heat of adsorption of hydrogen. *Trans. Faraday Soc.* **1957**, *54*, 1053–1063. [CrossRef]
165. Sabatier, P. Hydrogénation et déhydrogénations par catalyse. *Ber. Der Dtsch. Chem. Ges.* **1911**, *44*, 1984–2001. [CrossRef]
166. Roger, I.; Shipman, M.A.; Symes, M.D. Earth-abundant catalysts for electrochemical and photoelectrochemical water splitting. *Nat. Rev. Chem.* **2017**, *1*, 3. [CrossRef]
167. Skúlason, E.; Tripkovic, V.; Björketun, M.E.; Gudmundsdóttir, S.; Karlberg, G.; Rossmeisl, J.; Bligaard, T.; Jónsson, H.; Nørskov, J.K. Modeling the electrochemical hydrogen oxidation and evolution reactions on the basis of density functional theory calculations. *J. Phys. Chem. C* **2010**, *114*, 18182–18197. [CrossRef]
168. Li, C.; Baek, J.B. Recent Advances in Noble Metal (Pt, Ru, and Ir)-Based Electrocatalysts for Efficient Hydrogen Evolution Reaction. *ACS Omega* **2020**, *5*, 31–40. [CrossRef]
169. Cai, J.; Javed, R.; Ye, D.; Zhao, H.; Zhang, J. Recent progress in noble metal nanocluster and single atom electrocatalysts for the hydrogen evolution reaction. *J. Mater. Chem. A* **2020**, *8*, 22467–22487. [CrossRef]
170. Dubouis, N.; Grimaud, A. The hydrogen evolution reaction: From material to interfacial descriptors. *Chem. Sci.* **2019**, *10*, 9165–9181. [CrossRef] [PubMed]
171. Zheng, J.; Sheng, W.; Zhuang, Z.; Xu, B.; Yan, Y. Universal dependence of hydrogen oxidation and evolution reaction activity of platinum-group metals on pH and hydrogen binding energy. *Sci. Adv.* **2016**, *2*, e1501602. [CrossRef] [PubMed]
172. Li, Z.; Ge, R.; Su, J.; Chen, L. Recent Progress in Low Pt Content Electrocatalysts for Hydrogen Evolution Reaction. *Adv. Mater. Interfaces* **2020**, *7*, 2000396. [CrossRef]
173. Duan, S.; Du, Z.; Fan, H.; Wang, R. Nanostructure optimization of platinum-based nanomaterials for catalytic applications. *Nanomaterials* **2018**, *8*, 949. [CrossRef] [PubMed]
174. Marković, N.M.; Sarraf, S.T.; Gasteiger, H.A.; Ross, P.N. Hydrogen electrochemistry on platinum low-index single-crystal surfaces in alkaline solution. *J. Chem. Soc. Faraday Trans.* **1996**, *92*, 3719–3725. [CrossRef]
175. Gilroy, K.D.; Farzinpour, P.; Sundar, A.; Hughes, R.A.; Neretina, S. Sacrificial templates for galvanic replacement reactions: Design criteria for the synthesis of pure Pt nanoshells with a smooth surface morphology. *Chem. Mater.* **2014**, *26*, 3340–3347. [CrossRef]

176. Zhao, Z.; Liu, H.; Gao, W.; Xue, W.; Liu, Z.; Huang, J.; Pan, X.; Huang, Y. Surface-Engineered PtNi-O Nanostructure with Record-High Performance for Electrocatalytic Hydrogen Evolution Reaction. *J. Am. Chem. Soc.* **2018**, *140*, 9046–9050. [\[CrossRef\]](#)
177. Zhang, Z.; Liu, G.; Cui, X.; Chen, B.; Zhu, Y.; Gong, Y.; Saleem, F.; Xi, S.; Du, Y.; Borgna, A.; et al. Crystal Phase and Architecture Engineering of Lotus-Thalamus-Shaped Pt-Ni Anisotropic Superstructures for Highly Efficient Electrochemical Hydrogen Evolution. *Adv. Mater.* **2018**, *30*, 1801741. [\[CrossRef\]](#)
178. Koo, B.; Chu, J.; Seo, J.; Jung, G.; Baek, S.H.; Nam, S.W.; Duah, C.; Lee, Y.K.; Jung, W.C.; Shin, B. Drop-casted Platinum Nanocube Catalysts for Hydrogen Evolution Reaction with Ultrahigh Mass Activity. *ChemSusChem* **2021**, *14*, 2585–2590. [\[CrossRef\]](#)
179. Liu, L.; Corma, A. Metal Catalysts for Heterogeneous Catalysis: From Single Atoms to Nanoclusters and Nanoparticles. *Chem. Rev.* **2018**, *118*, 4981–5079. [\[CrossRef\]](#)
180. Wang, H.; Lu, J. A Review on Particle Size Effect in Metal-Catalyzed Heterogeneous Reactions. *Chin. J. Chem.* **2020**, *38*, 1422–1444. [\[CrossRef\]](#)
181. Zhang, J.; Zhao, Y.; Guo, X.; Chen, C.; Dong, C.L.; Liu, R.S.; Han, C.P.; Li, Y.; Gogotsi, Y.; Wang, G. Single platinum atoms immobilized on an MXene as an efficient catalyst for the hydrogen evolution reaction. *Nat. Catal.* **2018**, *1*, 985–992. [\[CrossRef\]](#)
182. Yu, P.-W.; Elmas, S.; Roman, T.; Pan, X.; Yin, Y.; Gibson, C.T.; Andersson, G.G.; Andersson, M.R. Highly Active Platinum Single-Atom Catalyst Grafted onto 3D Carbon Cloth Support for the Electrocatalytic Hydrogen Evolution Reaction. *Appl. Surf. Sci.* **2022**, *595*, 153480. [\[CrossRef\]](#)
183. Elmas, S.; Beelders, W.; Bradley, S.J.; Kroon, R.; Laufersky, G.; Andersson, M.; Nann, T. Platinum Terpyridine Metallopolymer Electrode as Cost-Effective Replacement for Bulk Platinum Catalysts in Oxygen Reduction Reaction and Hydrogen Evolution Reaction. *ACS Sustain. Chem. Eng.* **2017**, *5*, 10206–10214. [\[CrossRef\]](#)
184. Cheng, N.; Stambula, S.; Wang, D.; Banis, M.N.; Liu, J.; Riese, A.; Xiao, B.; Li, R.; Sham, T.K.; Liu, L.M.; et al. Platinum single-atom and cluster catalysis of the hydrogen evolution reaction. *Nat. Commun.* **2016**, *7*, 13638. [\[CrossRef\]](#)
185. Sun, S.; Zhang, G.; Gauquelin, N.; Chen, N.; Zhou, J.; Yang, S.; Chen, W.; Meng, X.; Geng, D.; Banis, M.N.; et al. Single-atom catalysis using Pt/graphene achieved through atomic layer deposition. *Sci. Rep.* **2013**, *3*, 1775. [\[CrossRef\]](#)
186. Shi, Y.; Ma, Z.R.; Xiao, Y.Y.; Yin, Y.C.; Huang, W.M.; Huang, Z.C.; Zheng, Y.Z.; Mu, F.Y.; Huang, R.; Shi, G.Y.; et al. Electronic metal-support interaction modulates single-atom platinum catalysis for hydrogen evolution reaction. *Nat. Commun.* **2021**, *12*, 3021. [\[CrossRef\]](#)
187. Tavakkoli, M.; Holmberg, N.; Kronberg, R.; Jiang, H.; Sainio, J.; Kauppinen, E.I.; Kallio, T.; Laasonen, K.; Tavakkoli, M.; Holmberg, N.; et al. Electrochemical activation of single-walled carbon nanotubes with pseudo atomic-scale platinum for hydrogen evolution reaction. *ACS Catal.* **2017**, *7*, 3121–3130. [\[CrossRef\]](#)
188. Pu, Z.; Amiin, I.S.; Cheng, R.; Wang, P.; Zhang, C.; Mu, S.; Zhao, W.; Su, F.; Zhang, G.; Liao, S.; et al. Single-Atom Catalysts for Electrochemical Hydrogen Evolution Reaction: Recent Advances and Future Perspectives. *Nano-Micro Lett.* **2020**, *12*, 21. [\[CrossRef\]](#)
189. Fang, S.; Zhu, X.; Liu, X.; Gu, J.; Liu, W.; Wang, D.; Zhang, W.; Lin, Y.; Lu, J.; Wei, S.; et al. Uncovering near-free platinum single-atom dynamics during electrochemical hydrogen evolution reaction. *Nat. Commun.* **2020**, *11*, 1029. [\[CrossRef\]](#)
190. Xiong, B.Y.; Xia, Y. Shape-Controlled Synthesis of Metal Nanostructures: The Case of Palladium. *Adv. Mater.* **2007**, *19*, 3385–3391. [\[CrossRef\]](#)
191. Wang, Y.; Xie, S.; Liu, J.; Park, J.; Huang, C.Z.; Xia, Y. Shape-Controlled Synthesis of Palladium Nanocrystals: A Mechanistic Understanding of the Evolution from Octahedrons to Tetrahedrons. *Nano Lett.* **2013**, *13*, 2276–2281. [\[CrossRef\]](#)
192. Janssen, A.; Shi, Y.; Xia, Y. Separating Growth from Nucleation for Facile Control over the Size and Shape of Palladium Nanocrystals. *Chem. A Eur. J.* **2020**, *26*, 13890–13895. [\[CrossRef\]](#) [\[PubMed\]](#)
193. Zalineeva, A.; Baranton, S.; Coutanceau, C.; Jerkiewicz, G. Octahedral palladium nanoparticles as excellent hosts for electrochemically adsorbed and absorbed hydrogen. *Sci. Adv.* **2017**, *3*, e1600542. [\[CrossRef\]](#) [\[PubMed\]](#)
194. Li, J.; Li, F.; Guo, S.X.; Zhang, J.; Ma, J. PdCu@Pd Nanocube with Pt-like Activity for Hydrogen Evolution Reaction. *ACS Appl. Mater. Interfaces* **2017**, *9*, 8151–8160. [\[CrossRef\]](#) [\[PubMed\]](#)
195. Wang, G.; Liu, J.; Sui, Y.; Wang, M.; Qiao, L.; Du, F.; Zou, B. Palladium structure engineering induced by electrochemical H intercalation boosts hydrogen evolution catalysis. *J. Mater. Chem. A* **2019**, *7*, 14876–14881. [\[CrossRef\]](#)
196. Liang, Z.; Ahn, H.S.; Bard, A.J. A Study of the Mechanism of the Hydrogen Evolution Reaction on Nickel by Surface Interrogation Scanning Electrochemical Microscopy. *J. Am. Chem. Soc.* **2017**, *139*, 4854–4858. [\[CrossRef\]](#)
197. Vij, V.; Sultan, S.; Harzandi, A.M.; Meena, A.; Tiwari, J.N.; Lee, W.G.; Yoon, T.; Kim, K.S. Nickel-based electrocatalysts for energy-related applications: Oxygen reduction, oxygen evolution, and hydrogen evolution reactions. *ACS Catal.* **2017**, *7*, 7196–7225. [\[CrossRef\]](#)
198. Li, Z.; Yu, C.; Wen, Y.; Gao, Y.; Xing, X.; Wei, Z.; Sun, H.; Zhang, Y.W.; Song, W. Mesoporous Hollow Cu-Ni Alloy Nanocage from Core-Shell Cu@Ni Nanocube for Efficient Hydrogen Evolution Reaction. *ACS Catal.* **2019**, *9*, 5084–5095. [\[CrossRef\]](#)
199. Fu, M.; Zhang, Q.; Sun, Y.; Ning, G.; Fan, X.; Wang, H.; Lu, H.; Zhang, Y.; Wang, H. Ni-Fe nanocubes embedded with Pt nanoparticles for hydrogen and oxygen evolution reactions. *Int. J. Hydrog. Energy* **2020**, *45*, 20832–20842. [\[CrossRef\]](#)
200. Hong, Y.; Choi, C.H.; Choi, S.-I. Catalytic Surface Specificity of Ni(OH)₂-Decorated Pt Nanocubes for the Hydrogen Evolution Reaction in an Alkaline Electrolyte. *ChemSusChem* **2019**, *12*, 4021–4028. [\[CrossRef\]](#) [\[PubMed\]](#)

201. Kavian, R.; Choi, S.-I.; Park, J.; Liu, T.; Peng, H.C.; Lu, N.; Wang, J.; Kim, M.J.; Xia, Y.; Lee, S.W. Pt-Ni octahedral nanocrystals as a class of highly active electrocatalysts toward the hydrogen evolution reaction in an alkaline electrolyte. *J. Mater. Chem. A* **2016**, *4*, 12392–12397. [CrossRef]
202. Seo, B.; Baek, D.S.; Sa, Y.J.; Joo, S.H. Shape effects of nickel phosphide nanocrystals on hydrogen evolution reaction. *CrystEngComm* **2016**, *18*, 6083–6089. [CrossRef]
203. Xiang, D.; Zhang, B.; Zhang, H.; Shen, L. One-Step Synthesis of Bifunctional Nickel Phosphide Nanowires as Electrocatalysts for Hydrogen and Oxygen Evolution Reactions. *Front. Chem.* **2021**, *9*, 773018. [CrossRef]
204. Li, R.; Li, C. *Photocatalytic Water Splitting on Semiconductor-Based Photocatalysts*, 1st ed.; Elsevier Inc.: Amsterdam, The Netherlands, 2017; Volume 60.
205. Li, X.; Wang, Z.; Wang, L. Metal–Organic Framework-Based Materials for Solar Water Splitting. *Small Sci.* **2021**, *1*, 2000074. [CrossRef]
206. Qiao, M.; Liu, J.; Wang, Y.; Li, Y.; Chen, Z. PdSeO₃ Monolayer: Promising Inorganic 2D Photocatalyst for Direct Overall Water Splitting Without Using Sacrificial Reagents and Cocatalysts. *J. Am. Chem. Soc.* **2018**, *140*, 12256–12262. [CrossRef]
207. Jafari, T.; Moharreri, E.; Amin, A.S.; Miao, R.; Song, W.; Suib, S.L. Photocatalytic water splitting—The untamed dream: A review of recent advances. *Molecules* **2016**, *21*, 900. [CrossRef]
208. Hisatomi, T.; Domen, K. Reaction systems for solar hydrogen production via water splitting with particulate semiconductor photocatalysts. *Nat. Catal.* **2019**, *2*, 387–399. [CrossRef]
209. Fujishima, A.; Honda, K. Electrochemical Photolysis of Water at a Semiconductor Electrode. *Nature* **1972**, *238*, 37–38. [CrossRef]
210. Teixeira, I.F.; Barbosa, E.C.M.; Tsang, S.C.E.; Camargo, P.H.C. Carbon nitrides and metal nanoparticles: From controlled synthesis to design principles for improved photocatalysis. *Chem. Soc. Rev.* **2018**, *47*, 7783–7817. [CrossRef]
211. Prasad, S.; Schumacher, H.; Gopinath, A. *Review of Semiconductor Materials and Physics*; Cambridge University Press: Cambridge, UK, 2010; ISBN 9780511626517. [CrossRef]
212. Chou, H.L.; Hwang, B.J.; Sun, C.L. *Catalysis in Fuel Cells and Hydrogen Production*; Elsevier B.V.: Amsterdam, The Netherlands, 2013; ISBN 9780444538802.
213. Ismail, A.A.; Bahnemann, D.W. Photochemical splitting of water for hydrogen production by photocatalysis: A review. *Sol. Energy Mater. Sol. Cells* **2014**, *128*, 85–101. [CrossRef]
214. Zhu, Y.X.; Jiang, M.Y.; Liu, M.; Wu, L.K.; Hou, G.Y.; Tang, Y.P. An Fe-V@NiO heterostructure electrocatalyst towards the oxygen evolution reaction. *Nanoscale* **2020**, *12*, 3803–3811. [CrossRef] [PubMed]
215. Niu, Z.; Qiu, C.; Jiang, J.; Ai, L. Hierarchical CoP-FeP Branched Heterostructures for Highly Efficient Electrocatalytic Water Splitting. *ACS Sustain. Chem. Eng.* **2019**, *7*, 2335–2342. [CrossRef]
216. Shit, S.; Chhetri, S.; Jang, W.; Murmu, N.C.; Koo, H.; Samanta, P.; Kuila, T. Cobalt Sulfide/Nickel Sulfide Heterostructure Directly Grown on Nickel Foam: An Efficient and Durable Electrocatalyst for Overall Water Splitting Application. *ACS Appl. Mater. Interfaces* **2018**, *10*, 27712–27722. [CrossRef] [PubMed]
217. Shit, S.; Chhetri, S.; Bolar, S.; Murmu, N.C.; Jang, W.; Koo, H.; Kuila, T. Hierarchical Cobalt Sulfide/Molybdenum Sulfide Heterostructure as Bifunctional Electrocatalyst towards Overall Water Splitting. *ChemElectroChem* **2019**, *6*, 430–438. [CrossRef]
218. Zhang, H.; Maijenburg, A.W.; Li, X.; Schweizer, S.L.; Wehrspohn, R.B. Bifunctional Heterostructured Transition Metal Phosphides for Efficient Electrochemical Water Splitting. *Adv. Funct. Mater.* **2020**, *30*, 2003261. [CrossRef]
219. Sitara, E.; Nasir, H.; Mumtaz, A.; Ehsan, M.F.; Sohail, M.; Iram, S.; Bukhari, S.A.B. Efficient photoelectrochemical water splitting by tailoring MoS₂/CoTe heterojunction in a photoelectrochemical cell. *Nanomaterials* **2020**, *10*, 2341. [CrossRef]
220. Lucas, T.T.A.; Melo, M.A.; Freitas, A.L.M.; Souza, F.L.; Gonçalves, R.V. Enhancing the solar water splitting activity of TiO₂ nanotube-array photoanode by surface coating with La-doped SrTiO₃. *Sol. Energy Mater. Sol. Cells* **2020**, *208*, 110428. [CrossRef]
221. Ge, J.; Liu, Y.; Jiang, D.; Zhang, L.; Du, P. Integrating non-precious-metal cocatalyst Ni₃N with g-C₃N₄ for enhanced photocatalytic H₂ production in water under visible-light irradiation. *Cuihua Xuebao/Chin. J. Catal.* **2019**, *40*, 160–167. [CrossRef]
222. Ma, S.; Deng, Y.; Xie, J.; He, K.; Liu, W.; Chen, X.; Li, X. Noble-metal-free Ni₃C cocatalysts decorated CdS nanosheets for high-efficiency visible-light-driven photocatalytic H₂ evolution. *Appl. Catal. B Environ.* **2018**, *227*, 218–228. [CrossRef]
223. Shen, R.; Xie, J.; Xiang, Q.; Chen, X.; Jiang, J.; Li, X. Ni-based photocatalytic H₂-production cocatalysts. *Cuihua Xuebao/Chin. J. Catal.* **2019**, *40*, 240–288. [CrossRef]
224. Li, Z.; Ma, Y.; Hu, X.; Liu, E.; Fan, J. Enhanced photocatalytic H₂ production over dual-cocatalyst-modified g-C₃N₄ heterojunctions. *Cuihua Xuebao/Chin. J. Catal.* **2019**, *40*, 434–445. [CrossRef]
225. Fujishima, A.; Kohayakawa, K.; Honda, K. Hydrogen Production under Sunlight with an Electrochemical Photocell. *J. Electrochem. Soc.* **1975**, *122*, 1487–1489. [CrossRef]
226. Chandra, M.; Pradhan, D. Engineering the Morphology and Crystal Phase of 3D Hierarchical TiO₂ with Excellent Photochemical and Photoelectrochemical Solar Water Splitting. *ChemSusChem* **2020**, *13*, 3005–3016. [CrossRef]
227. Peng, Y.W.; Shan, C.; Wang, H.J.; Hong, L.Y.; Yao, S.; Wu, R.J.; Zhang, Z.M.; Lu, T.B. Polyoxometalate-Derived Ultrasmall Pt₂W/WO₃ Heterostructure Outperforms Platinum for Large-Current-Density H₂ Evolution. *Adv. Energy Mater.* **2019**, *9*, 1900597. [CrossRef]
228. Zhao, G.; Li, P.; Cheng, N.; Dou, S.X.; Sun, W. An Ir/Ni(OH)₂ Heterostructured Electrocatalyst for the Oxygen Evolution Reaction: Breaking the Scaling Relation, Stabilizing Iridium(V), and Beyond. *Adv. Mater.* **2020**, *32*, 2000872. [CrossRef]

229. Xu, J.; Zhang, C.; Liu, H.; Sun, J.; Xie, R.; Qiu, Y.; Lü, F.; Liu, Y.; Zhuo, L.; Liu, X.; et al. Amorphous MoOX-Stabilized single platinum atoms with ultrahigh mass activity for acidic hydrogen evolution. *Nano Energy* **2020**, *70*, 104529. [[CrossRef](#)]
230. Yi, S.S.; Zhang, X.B.; Wulan, B.R.; Yan, J.M.; Jiang, Q. Non-noble metals applied to solar water splitting. *Energy Environ. Sci.* **2018**, *11*, 3128–3156. [[CrossRef](#)]
231. Li, T.; Ding, D.; Dong, Z.; Ning, C. Photoelectrochemical water splitting properties of Ti-Ni-Si-O nanostructures on Ti-Ni-Si alloy. *Nanomaterials* **2017**, *7*, 359. [[CrossRef](#)]
232. Singh, S.B. Nanomaterials for Water Splitting: A Greener Approach to Generate Hydrogen. In *Nanomaterials for Water Splitting: A Greener Approach to Generate Hydrogen*; Springer: Cham, Denmark, 2021; pp. 1201–1220.
233. Grewe, T.; Meggouh, M.; Tüysüz, H. Nanocatalysts for Solar Water Splitting and a Perspective on Hydrogen Economy. *Chem. Asian J.* **2016**, *11*, 22–42. [[CrossRef](#)]
234. da Silva, A.G.M.; Rodrigues, T.S.; Candido, E.G.; de Freitas, I.C.; da Silva, A.H.M.; Fajardo, H.V.; Balzer, R.; Gomes, J.F.; Assaf, J.M.; de Oliveira, D.C.; et al. Combining active phase and support optimization in MnO₂-Au nanoflowers: Enabling high activities towards green oxidations. *J. Colloid Interface Sci.* **2018**, *530*, 282–291. [[CrossRef](#)] [[PubMed](#)]
235. da Silva, A.G.M.; Rodrigues, T.S.; Macedo, A.; da Silva, R.T.P.; Camargo, P.H.C. An Undergraduate Level Experiment on the Synthesis of Au Nanoparticles and Their Size-Dependent Optical and Catalytic Properties. *Quim. Nov.* **2014**, *37*, 1716–1720. [[CrossRef](#)]
236. Lu, M.; Cui, X.; Song, B.; Ouyang, H.; Wang, K.; Wang, Y. Studying the Effect of CuCo₂S₄ Morphology on the Oxygen Evolution Reaction using a Flexible Carbon Cloth Substrate. *ChemElectroChem* **2020**, *7*, 1080–1083. [[CrossRef](#)]
237. Fang, L.; Jiang, Z.; Xu, H.; Liu, L.; Guan, Y.; Gu, X.; Wang, Y. Crystal-plane engineering of NiCo₂O₄ electrocatalysts towards efficient overall water splitting. *J. Catal.* **2018**, *357*, 238–246. [[CrossRef](#)]
238. Li, Y.; Sun, Y.; Qin, Y.; Zhang, W.; Wang, L.; Luo, M.; Yang, H.; Guo, S. Recent Advances on Water-Splitting Electrocatalysis Mediated by Noble-Metal-Based Nanostructured Materials. *Adv. Energy Mater.* **2020**, *10*, 1903120. [[CrossRef](#)]
239. da Silva, A.G.M.; Fernandes, C.G.; Hood, Z.D.; Peng, R.; Wu, Z.; Dourado, A.H.B.; Parreira, L.S.; de Oliveira, D.C.; Camargo, P.H.C.; de Torresi, S.I.C. PdPt-TiO₂ nanowires: Correlating composition, electronic effects and O-vacancies with activities towards water splitting and oxygen reduction. *Appl. Catal. B Environ.* **2020**, *277*, 119177. [[CrossRef](#)]
240. Zheng, D.; Cao, X.; Wang, X. Precise Formation of a Hollow Carbon Nitride Structure with a Janus Surface To Promote Water Splitting by Photoredox Catalysis. *Angew. Chem.* **2016**, *128*, 11684–11688. [[CrossRef](#)]
241. Wei, Z.; Mogan, T.R.; Wang, K.; Janczarek, M.; Kowalska, E. Morphology-governed performance of multi-dimensional photocatalysts for hydrogen generation. *Energies* **2021**, *14*, 7223. [[CrossRef](#)]
242. Samuel, E.; Joshi, B.; Kim, M.W.; Swihart, M.T.; Yoon, S.S. Morphology engineering of photoelectrodes for efficient photoelectrochemical water splitting. *Nano Energy* **2020**, *72*, 104648. [[CrossRef](#)]
243. Yue, M.; Lambert, H.; Pahon, E.; Roche, R.; Jemei, S.; Hissel, D. Hydrogen energy systems: A critical review of technologies, applications, trends and challenges. *Renew. Sustain. Energy Rev.* **2021**, *146*, 111180. [[CrossRef](#)]
244. Grigoriev, S.A.; Fateev, V.N.; Bessarabov, D.G.; Millet, P. Current status, research trends, and challenges in water electrolysis science and technology. *Int. J. Hydrog. Energy* **2020**, *45*, 26036–26058. [[CrossRef](#)]
245. Wang, Q.; Hisatomi, T.; Jia, Q.; Tokudome, H.; Zhong, M.; Wang, C.; Pan, Z.; Takata, T.; Nakabayashi, M.; Shibata, N.; et al. Scalable water splitting on particulate photocatalyst sheets with a solar-to-hydrogen energy conversion efficiency exceeding 1%. *Nat. Mater.* **2016**, *15*, 611–615. [[CrossRef](#)] [[PubMed](#)]
246. Moss, R.; Tzimas, E.; Willis, P.; Arendorf, J.; Tercero Espinoza, L. *Critical Metals in the Path towards the Decarbonisation of the EU Energy Sector: Assessing Rare Metals as Supply-Chain Bottlenecks in Low-Carbon Energy Technologies*; Publications Office of the European Union: Luxembourg, 2013.